Author/s:
Phillips, D;Matchan, E;Gleadow, A;Brown, F;McDougall, I;Cerling, T;Leakey, M;Hergt, J;Leakey, L

Title:
40Ar/39Ar eruption ages of Turkana Basin tuffs: millennial scale resolution constrains paleoclimate proxy tuning models and hominin fossil ages

Date:
2023

Citation:
Phillips, D., Matchan, E., Gleadow, A., Brown, F., McDougall, I., Cerling, T., Leakey, M., Hergt, J. & Leakey, L. (2023). 40Ar/39Ar eruption ages of Turkana Basin tuffs: millennial scale resolution constrains paleoclimate proxy tuning models and hominin fossil ages. Journal of the Geological Society, 180 (4), https://doi.org/10.1144/jgs2022-171.

Persistent Link:
https://hdl.handle.net/11343/330131

Accepted Manuscript

Journal of the Geological Society

$^{40}Ar/^{39}Ar$ eruption ages of Turkana Basin tuffs: millennial scale resolution constrains paleoclimate proxy tuning models and hominin fossil ages

David Phillips, Erin Matchan, Andy Gleadow, Frank Brown, Ian McDougall, Thure Cerling, Meave Leakey, Janet Hergt & Louise Leakey

DOI: https://doi.org/10.1144/jgs2022-171

To access the most recent version of this article, please click the DOI URL in the line above. When citing this article please include the above DOI.

Received 5 December 2022
Revised 29 March 2023
Accepted 29 March 2023

Supplementary material at https://doi.org/10.6084/m9.figshare.c.6602994

$^{40}Ar/^{39}Ar$ eruption ages of Turkana Basin tuffs: millennial scale resolution constrains paleoclimate proxy tuning models and hominin fossil ages

David Phillips[1*], Erin Matchan[1], Andy Gleadow[1], Frank Brown[2†], Ian McDougall[3†]. Thure Cerling[4], Meave Leakey[5], Janet Hergt[1] and Louise Leakey[5]

[1]School of Geography, Earth and Atmospheric Sciences, The University of Melbourne, Parkville, VIC, 3010, Australia

[2]Department of Geology and Geophysics, University of Utah, USA

[3]Research School of Earth Sciences, The Australian National University, Canberra, Australia

[4]Department of Geology and Geophysics, University of Utah, USA

[5]Turkana Basin Institute, Department of Social and Behavioural Sciences, Stony Brook University, Stony Brook, NY, 11794-4364

[†](Deceased)

*Corresponding author: David Phillips.

Email: dphillip@unimelb.edu.au

Keywords: Turkana Basin**,** volcanic tuff, $^{40}Ar/^{39}Ar$ geochronology, hominin evolution**,** paleoclimate.

Abstract: The Turkana Basin in Kenya/Ethiopia hosts remarkable fossil-rich sediments that are central to our understanding of early hominin evolution, with interbedded volcanic tuffs providing critical time markers. However, the resolution of existing Early Pleistocene/Pliocene ages is limited to ~20-60 kyr, inhibiting evaluation of climatic/environmental drivers of evolution. Here, we present high precision, single-feldspar $^{40}Ar/^{39}Ar$ age and elemental data for four stratigraphically significant tuffs. These samples exhibit variably dispersed age distributions correlated with feldspar compositional trends, interpreted to indicate partial retention of inherited argon, related to crustal 'cold storage' and rapid melt infiltration preceding eruption. We evaluated various statistical methods and calculate astronomically calibrated, Bayesian age estimates of 1879.1 ± 0.6 ka (± 2.4 ka including external errors) for the KBS/H2 Tuff, 1837.4 ± 0.9 ka (± 2.4 ka) for the Malbe/H4 Tuff, 1357.5 ± 1.8 ka (± 2.5 ka) for the Chari/L Tuff and 1315.4 ± 1.9 ka (± 2.5 ka) for the Gele Tuff. Our results permit refined age constraints for important early *Homo* fossils, including the cranium KNM-ER1813 (*Homo habilis*) and various *Homo erectus* fossils. The KBS Tuff age also provides an important calibration locus for orbital tuning of paleoclimate proxy records, revealing complex interplay between paleoclimate and geological drivers of sedimentation.

Introduction

Questions on the origin of our species (*Homo sapiens*) have captivated humankind for decades. Hominin fossils unearthed following the 1924 discovery of the early hominin *Taung* skull (*Australopithecus africanus*) in South Africa (Dart 1925) have afforded remarkable insights into the antiquity (>4.3 Ma) and complexity of human evolution (e.g. Wood and Leakey 2011; Anton et al. 2014). Important hominin fossil sites are now known from South Africa (e.g. Sterkfontein, Malapa), East Africa (e.g. Olduvai Gorge, Turkana Basin, Middle Awash, Konso), northern Chad and Eurasia (e.g. Dmanisi).

The Turkana Basin in northwest Kenya and southwest Ethiopia (Fig. 1) is particularly significant owing to a combination of extensive fossiliferous sedimentary sequences that record much of early human evolution, and an abundance of intercalated silicic tuffs (plus key geomagnetic excursions) that provide critical time constraints (e.g. McDougall and Brown, 2006, 2008; McDougall et al. 2012). However, most Early Pleistocene/Pliocene tuffs have associated $^{40}Ar/^{39}Ar$ age uncertainties >20 ka (McDougall & Brown, 2006; 2008; McDougall et al. 2012), and age estimates for key geomagnetic excursions such as the base of the Olduvai Subchron (bC2n: 1925 to 1968 ka; Δ = 43 kyr) are contentious (Channell et al. 2020). These uncertainties inhibit the temporal distinction of closely spaced tuffs (e.g. units within the Chari Member; McDougall and Brown 2006), as well as millennial-scale orbital tuning of sedimentary paleoclimate cycles (e.g. Joordens et al. 2011, 2013; Lupien et al. 2018, 2020), and finer-scale resolution of the fossil records. The key to resolving these issues is a higher resolution chronological framework for Turkana Basin tuffs (e.g. Levin, 2015).

The order of magnitude improvement in analytical precision afforded by new generation, multi-collector mass spectrometers should permit millennial-scale resolution of Turkana Basin tuffs. However, the increased precision also reveals previously unrecognised age heterogeneities, thereby complicating age assignment. In a number of previous studies, feldspars from volcanic tuffs have produced $^{40}Ar^*/^{39}Ar$ age distributions with 'tails' towards distinctly older (and sometimes younger) ages (e.g. Lo Bello et al. 1987; van den Bogaard et al. 1989; Andersen et al. 2017; Yancy et al., 2018; van Zalinge et al. 2022). The older ages are conventionally attributed to the presence of feldspar xenocrysts, antecrysts and extraneous (i.e. excess or inherited) argon, although recent studies have invoked low-temperature storage of crystal cargoes

and partial retention of inherited argon (e.g. Andersen et al. 2017; van Zalinge et al. 2022). Younger feldspar ages are usually ascribed to argon loss and/or irradiation/analytical artefacts (e.g. Phillips and Matchan, 2013; Andersen et al. 2017). The revelation of such dispersed $^{40}Ar/^{39}Ar$ age distributions has necessitated a re-evaluation of how best to extract eruption ages from these datasets (e.g. Schaen et al. 2020 and references therein).

In this study, we focus on four paleoanthropologically important Turkana Basin tuffs, each characterized by distinct $^{40}Ar/^{39}Ar$ feldspar age distributions: the ~1.9 Ma Kay Behrensmeyer Site (KBS) (=H2 Tuff, Shungura Formation) and Malbe (=H4 Tuff, Shungura Fm) tuffs and the ~1.3 Ma Chari (= Tuff L, Shungura Fm) and Gele tuffs in the Koobi Fora Formation (Fig. 1). The $^{40}Ar/^{39}Ar$ results are complemented by elemental data from pumice glass, tuff glass and pumice feldspars, which are used to verify pumice attribution to host tuffs and provide insights into the complexities of source magma dynamics. We utilise a range of statistical approaches to estimate tuff eruption ages, before comparing our results with previously published ages. Finally, we utilise the eruption age results to test paleoclimate proxy interpretations for strata below the KBS Tuff and update age constraints for associated hominin fossils.

Geological setting

The Turkana Basin formed *ca.* 4.3 Myr ago and is dominated by Plio-Pleistocene river, delta and lake sediments, mostly drained from the Ethiopian highlands to the north (Fig. 1). Originally mapped as three separate formations, sediments of the Koobi Fora (~560 m thick), Nachukui (~730 m thick) and Shungura Formations (~766 m thick) are now known to be contemporaneous and are collated within the Omo Group (de Heizelin 1983; Brown and Feibel 1986; Harris et al. 1988). Ash beds in the Omo Group and Konso Formation, Ethiopia, are thought to be sourced from volcanic centres within the axial zone of the Main Ethiopian Rift (MER) (WoldeGabriel et al. 2005), but the source volcanic centres have yet to be identified. Although some ash fall deposits have been reported, most tuffs in the Basin were formed by fluvial transport and deposition of ash (e.g. McDougall and Brown 2006, 2008). The generally sharp basal contacts between the tuffs and underlying sediments, and limited contamination with detrital sedimentary material, indicate a short timespan between eruption and ash deposition in the Basin (McDougall and Brown 2006, 2008). Several ash beds, such the KBS Tuff, are

regionally extensive, whereas others (e.g. Gele Tuff) only occur locally (Cerling and Brown 1982; Brown et al. 2006).

A number of Turkana Basin tuffs contain pumice clasts that host feldspar (typically anorthoclase) crystals, which are the primary target for $^{40}Ar/^{39}Ar$ geochronology. Ages are available for some 40 Omo Group tuffs, ranging from 4.23 ± 0.01 (2σ) Ma (unnamed tuff, Apak Member, Nachukui Fm) to 0.750 ± 0.006 (2σ) Ma (Silbo tuff, Chari Member, Koobi Fora Formation) (McDougall and Brown 2006, 2008) (Fig. 1).

The first tuff to be identified in the Turkana Basin was the KBS Tuff, which defines the lower boundary of the KBS Member (Brown et al. 2006) (Fig. 1). The type locality of the KBS tuff is archaeological discovery site FxJj1 in Palaeontological Collection Area 105 of the Koobi Fora region. Along the Koobi Fora and Karari ridges, the KBS Tuff occurs in a sequence of lacustrine and fluvial sediments, although airfall ash has been described from areas 102, 107 and 110 (Brown et al. 2006). Altered KBS tuff outcrops also occur at several localities in the Nachukui Formation, west of Lake Turkana (Brown et al. 2006). The H2 tuff in the Shungura Formation, Ethiopia, is correlated with the KBS tuff on the basis of geochemistry (Cerling et al. 1979) and age data (Drake et al. 1980) (Fig. 1) and occurs as a ~0.4m thick unit containing pumice clasts up to 40cm diameter (Brown et al. 2006). Although it has been suggested that the KBS (=H2) Tuff is correlated with the Turoha Tuff (TRT) in the Konso region (Katoh et al. 2000), Brown et al. (2006) note subtle differences in tuff geochemistry and question this correlation.

Initially misidentified as the KBS Tuff (Curtis et al. 1975), the stratigraphically younger Malbe Tuff outcrops in areas 102, 105, 106, and 112 at Koobi Fora and in the Nachukui Formation (Cerling et al. 1979; Cerling and Brown 1982; McDougall and Brown 2006). The H4 tuff in the type area of the Shungura Formation is correlated with the Malbe Tuff on the basis of geochemistry (Cerling et al. 1979) and age data (Drake et al. 1980) (Fig. 1). The Malbe Tuff is located ~15m above the KBS Tuff in the Koobi Fora (Feibel 1983; McDougall and Brown 2006) and Shungura formations (Cerling and Brown 1982).

The Chari Tuff defines the base of the Chari Member in the Koobi Fora Formation (Fig. 1) (Brown and Feibel 1985, 1986). The tuff is ~4.6 m thick in its type section (Area 5), but also occurs across the Ileret region and the Karari Ridge (Areas 131, 133, 128). The Chari Tuff contains abundant, large pumice clasts up to ~50 cm in diameter.

The tuff occurs as a relatively thin layer (~10 cm) in the Nachukui Formation (Harris et al. 1988) and was recently identified in the Hominin Sites and Paleolakes Drilling Project (HSPDP) WTK13 drill-core (Campisano et al. 2017). The Chari Tuff correlates with Tuff L in the Shuguru Formation (Fig. 1) and with the fall-out Bright White Tuff in the Konso region (Katoh et al. 2000).

The Gele Tuff, named by Feibel et al. (1989), has limited distribution, outcropping in Area 4 near the Ileret airstrip in the Koobi Fora Formation (Fig. 1). The tuff is ~0.5 m thick and is considered to be stratigraphically higher than the Chari Tuff on the basis of available $^{40}Ar/^{39}Ar$ age data (McDougall et al. 2006).

Previous geochronology

Previous geochronology results for the KBS (=H2), Malbe (=H4), Chari (=L) and Gele tuffs are summarized in Fig. 2 and Table S1. Ages reported in Table S1 include originally published values as well as recalculated ages based on the decay constants of Min et al. (2000) and the fluence monitor ages of Phillips et al. (2022). Ages plotted in Fig. 2 and discussed below are recalculated values with 2σ uncertainties.

Early attempts to date the KBS Tuff using K-Ar and $^{40}Ar/^{39}Ar$ analyses of bulk feldspar aliquots from entrained pumice clasts produced highly discrepant ages ranging from 2.67 ± 0.54 Ma (Fitch and Miller 1970) to 1.60 ± 0.10 Ma (Curtis et al. 1975) (Fig. 2; Table S1), sparking the so-called 'KBS Tuff Controversy' (see Lewin 1987). Subsequent K-Ar (Drake et al. 1980; McDougall et al. 1980; McDougall 1985), $^{40}Ar/^{39}Ar$ (McDougall 1981) and fission track (Gleadow 1980) studies produced consistent ages of ~1.88 Ma, largely ending the controversy. More recent $^{40}Ar/^{39}Ar$ analyses of single KBS pumice feldspar crystals yielded a precise weighted mean age of 1.873 ± 0.028 Ma (McDougall and Brown 2006), but with mean squared weighted deviate (MSWD) values for individual samples up to 12.1. This raised the possibility of age dispersion beyond analytical uncertainties, which is now clearly evident from multi-collector analyses. $^{40}Ar/^{39}Ar$ analyses of feldspars from the potentially correlated Turoha Tuff in the Konso region have a reported weighted mean age of 1.96 ± 0.06 Ma (Katoh et al. 2000), within uncertainty of the above KBS (=H2) results (Table S1).

Age assignment of the Malbe (=H4) Tuff has proved less contentious. Analyses of bulk pumice feldspar aliquots produced consistent K-Ar and $^{40}Ar/^{39}Ar$ ages of ca. 1.85 Ma (Drake et al. 1980; McDougall 1985; McDougall and Brown 2006); all within

uncertainty of reported KBS Tuff ages (Fig. 2). More recent analyses of single feldspar crystals from Malbe pumice clasts produced a reported a weighted mean $^{40}Ar/^{39}Ar$ age of 1.850 ± 0.012 Ma (McDougall and Brown 2006), again with elevated MSWD values (up to 15.3) for individual samples.

Reported K-Ar ages for the Chari (=L) Tuff are consistent at 1.39 ± 0.04 Ma and 1.39 ± 0.05 Ma (Drake et al. 1980; McDougall 1985), within uncertainty of a K-Ar age of 1.34 ± 0.14 Ma obtained from Tuff L samples (Brown and Nash 1976) and a weighted mean $^{40}Ar/^{39}Ar$ age (Chari Tuff samples) of 1.386 ± 0.010 Ma (MSWD values up to 28) (McDougall and Brown 2006). A marginally older $^{40}Ar/^{39}Ar$ age of 1.44 ± 0.04 Ma was obtained for the correlated Bright White Tuff in the Konso region (Katoh et al. 2000).

The age of the Gele Tuff is constrained by an imprecise K-Ar age of 1.25 ± 0.06 Ma (Brown et al. 1985) and an $^{40}Ar/^{39}Ar$ age of 1.331 ± 0.008 Ma (MSWD values up to 7.4; McDougall and Brown 2006).

Materials and Methods

Samples and sample preparation

A total of 19 feldspar-bearing, *in situ* pumice clast samples were selected for analysis from KBS/H2, Malbe/H4, Chari/Tuff L and Gele tuff localities across the Turkana Basin (Fig. 1; Table S2). The samples include six pumice clasts from five KBS/H2 tuff localities in areas 105 and 131 of the Koobi Fora Formation and one clast from the H2 Tuff type locality in the Shungura Formation. Five pumice clasts were recovered from two Malbe Tuff outcrops (Koobi Fora Fm)and one H4 Tuff locality (Shungura Fm) (Table S2). Four (~20 cm) pumice clasts were selected from three Chari Tuff exposure localities (Koobi Fora Fm), with one pumice clast collected from Tuff L (Shungura Fm). Three pumice samples were recovered from a single exposure of the Gele Tuff in Area 4, Koobi Fora Formation (Fig. 1, Table S2). In addition, a feldspar concentrate from Chari Tuff sample 81-219 (Area 1) was supplied by IM; this sample was analysed previously by McDougall and Brown (2006), yielding an age of 1.378 ± 0.012 Ma (2σ). Details of individual pumice samples are summarised in Table S2.

Pumice clasts collected in the field were initially scrubbed with a wire brush to remove weathered rinds. Each clast was then crushed manually, sieved, washed and dried. Feldspar crystals and glass shards were separated from all KBS/H2, Malbe/H4,

Chari/Tuff L and Gele pumice samples for $^{40}Ar/^{39}Ar$ dating and/or electron microprobe analyses. Grain mounts of tuff glass (samples ETH86-279, K80-225, K03-0069, K82-835; Brown et al. 2006; Gathogo and Brown 2006) were obtained from the University of Utah collection for electron microprobe re-analysis, to confirm the affinity of the pumice clasts to host tuffs (Table S3). Optically clear feldspar cleavage fragments (10-30 grains per sample) selected for $^{40}Ar/^{39}Ar$ analysis were hand-picked under a binocular microscope from either the 0.5–1 mm or 1–2 mm grainsize fractions, avoiding grains with obvious inclusions or signs of alteration. To remove undetected adherent glass or secondary minerals, feldspar grains were treated in an ultrasonic bath with 5% HNO_3 (5 min), 7% HF (10 min), deionised water (10 min), and acetone (3 min).

Major element analyses of feldspar and glass.

Feldspar crystals plus tuff and pumice glass fragments were mounted in Epoxy resin and analysed at the University of Melbourne using a JEOL JXA-8530F Field Emission Electron Probe Microanalyser (EPMA) (Tables S3, S4). Operating conditions included a beam accelerating voltage of 15 kV, beam current of 5 nA, beam diameter of 10 μm and counting times of 20 seconds on peaks and 10 seconds on two background positions either side of the peak, except for F and Na (10 s / 5 s) and Ba (40 s / 20 s). Data reduction was achieved using JEOL software with integrated ZAF matrix correction. Analysed standards included wollastonite (Si, Ca), aluminium oxide (Al), magnesium oxide (Mg), hematite (Fe), Mn metal (Mn), titanium oxide (Ti), K-tantalite (K), jadeite (Na), NaF (F), NaCl (Cl), TiZr (Zr) and benitoite (Ba).

EPMA analyses were conducted on volcanic glass fragments from all pumice clasts and representative tuff samples to confirm compositional affinity (Table S3; Fig. 3), as there is evidence of upward reworking in some instances (e.g., Morotut Tuff; McDougall and Brown, 2006). Tuff glass (and to a lesser extent pumice glass) fragments are often variably hydrated post-deposition, leading to relatively low EPMA totals (<96%) (Brown et al. 2006). Therefore, EPMA data shown in diagrams are normalised values based on 100% oxide totals. Brown et al. (2006) found that the least mobile elements include Ca, Fe, Ti, Al, Mn, Mg, Cl, Zr and Ba.

Three spots per feldspar grain (core/interior, intermediate, rim/exterior) were analysed for all KBS and Malbe samples, as well as Chari samples TB17-003-P2/P4,

whereas two analyses per grain (core/interior, rim/exterior) were conducted on the remaining Chari and Gele samples (Table S4). The presence or absence of compositional zonation was investigated using Ca- and Ba- contents (e.g. Iddon et al. 2019). A subset of Chari (=L) grains with relatively elevated core Ca- and Ba-concentrations were selected for line-scan analyses (Table S4).

^{40}Ar/^{39}Ar geochronology.

In preparation for neutron irradiation, feldspar grains were packaged into aluminium foil envelopes. To minimise neutron fluence gradients care was taken to ensure grains evenly surrounded a smaller (~3 mm diameter) aluminium foil envelope containing ~15 Fish Canyon Tuff sanidine (FCTs) crystals. The packets were then stacked coaxially in silica glass tubes and irradiated in either the CLICIT facility of the Oregon State University TRIGA (OSTR) reactor (UM#75 – 10 MWh; UM#77 – 20 MWh; UM#79 - 20 MWh; UM#85 - 4 MWh; UM#89 - 5 MWh; UM#94 - 6 MWh) or the U.S. Geological Survey's TRIGA reactor (UM#82 - 6 MWh).

^{40}Ar/^{39}Ar analyses were conducted at the University of Melbourne, using a multi-collector Thermo Fisher Scientific ARGUSVI mass spectrometer linked to a stainless-steel gas extraction/purification line and a Photon Machines Fusions 10.6 CO_2 laser system. Details of the ARGUSVI instrument are described in Phillips and Matchan (2013). In the current study, ^{36}Ar was measured on a Compact Discrete Dynode (CDD) detector, with the remaining argon isotopes measured on Faraday detectors (H1, AX, L1, L2) with low noise 1 x 10^{13} Ω resistors. Following neutron irradiation, feldspar crystals were loaded into copper sample holders and placed into the stainless-steel sample chamber with a ZnS cover slip. The extraction line was baked at ~90˚C until extraction line ^{40}Ar rate-of-rise levels had decreased to <1fA/min.

A number of samples in the current study contained relatively small (~0.5 mm) feldspar fragments with modest potassium contents (Fig. 2; Table S3), precluding precise step-heating analyses. Consequently, single grain, total fusion ^{40}Ar/^{39}Ar analyses were carried out on the majority of samples, although incremental heating analyses (2-4 steps) were conducted on larger feldspar crystals from KBS Tuff samples 7822-47A, 7822-38 and 77-107y. The main risk of this approach is a reduced capacity to recognise fragments affected by argon loss (e.g. Andersen et al., 2017; Deino et al.,

2019). However, our selection of optically clear feldspar fragments, and the lack of thermal overprints in the region, minimise this risk.

Air aliquots from an automated pipette system were analysed prior to sample analyses to monitor mass discrimination and detector bias. Gas introduced into the ARGUSVI mass spectrometer was equilibrated for 20s before multi-collector analysis of the five argon isotopes. Peak signals were collected for a period of 300s and linearly regressed to time zero (i.e., the time of gas inlet into the mass spectrometer). Extraction line blank behaviour was analogous to that described by Heizler et al. (2021). Mass 40 and 36 blanks stem mostly from the sample chamber and typically decrease after bakeout, with ^{40}Ar levels mostly <2 fA (Table S5). ^{40}Ar and ^{36}Ar Line blanks were measured before every 1 - 3 sample analyses, with correction values interpolated from bracketing blank measurements. ^{37}Ar, ^{38}Ar and ^{39}Ar blank levels were minimal, dominated by mass spectrometer contributions and generally time invariant. These blanks were either averaged across analytical cycles or interpolated where levels increased or decreased.

Interference correction values for all irradiations, based on analyses of irradiated K-glass and CaF_2 samples in associated (longer) irradiations, are listed in Table S5. Contributions from $^{36}Ar_{Cl}$ were calculated using the average of the $^{36}Cl/^{38}Cl$ production ratios (257.8 ± 2.5) reported for OSTR by Renne et al. (2008) and the $(^{36}Ar/^{38}Ar)_{Air}$ value (5.3050 ± 0.0084) of Lee et al. (2006). Apparent ages were calculated based on an astronomically tuned FCT sanidine age of 28.176 ± 0.011 Ma (± 0.032 Ma, including external uncertainties; Phillips et al., 2022) and the total K-decay constant of 5.463 ± 0.107 x 10^{-10} a^{-1} recommended by Min et al. (2000). Unless otherwise stated, age uncertainties are reported at the 2σ level and include uncertainties in the J-values. Full external uncertainties that include uncertainties in the astronomically calibrated age of FCTs and decay constants are reported with final ages.

$^{40}Ar/^{39}Ar$ data treatment

The current $^{40}Ar/^{39}Ar$ data were initially filtered to exclude a few analyses with very low argon yields (<20 fA), low radiogenic $^{40}Ar^*$ (<70%), anomalous blanks (> 2fA) or ^{39}Ar signals exceeding detector limits (Table S5). As the tuff feldspars produced variably dispersed $^{40}Ar/^{39}Ar$ data arrays (Table S5), eruption ages were estimated using

several statistical approaches trialled in recent studies (see review by Schaen et al. 2020; van Zalinge et al. 2022).

The first approach involves using a 'gap' algorithm to eliminate distinctly older ages, followed by data filtering via the normalized median absolute deviation (nMAD) method (e.g. Powell et al., 2020), thereby reducing scatter and enabling the calculation of a weighted mean age (e.g. Deino et al. 2019). This method assumes that the data have a normal (Gaussian) distribution, with older ages attributed to xenocryst/antecryst contamination and younger ages ascribed to argon loss or irradiation/analytical artefacts.

Schaen et al. (2020) summarise three alternative methods, here designated Models 1-3. Models 1 and 2 are based on the assumption that the youngest coherent age population most closely approximates the time of eruption. Model 1 (low MSWD weighted mean method) eruption ages are calculated from the youngest group of ages with an MSWD value less than the critical MSWD [= 1 + 2 * SQRT (2 / *f*); *f* = degrees of freedom]. Model 2 (weighted mean filter) involves calculating the youngest population with a weighted mean age that differs from the next oldest age at the 95% confidence level (e.g. Andersen et al., 2017). Model 3 (Normality test and goodness-of-fit filter) is based on the assumption that the eruption age is given by the largest subset of data that conform to a normal distribution, which may not include the youngest ages.

In contrast to the above methods, which attempt to extract or define a normal distribution from $^{40}Ar/^{39}Ar$ data arrays, van Zalinge et al. (2022) utilised a Bayesian estimation approach to calculate $^{40}Ar/^{39}Ar$ eruption ages, based on the algorithm used for U-Pb zircon age estimations (Keller et al. 2018). In this case, the authors showed that age arrays obtained from South American ignimbrites follow an exponential distribution, with $^{40}Ar/^{39}Ar$ Bayesian age estimates in general agreement with U-Pb zircon ages from the same volcanics.

Here, we apply all five approaches to the current data and compare resultant eruption age estimates. For the Bayesian age estimates, we used the interactive Jupyter notebook located at *https://github.com/brenhinkeller/BayeZirChron.c* (Keller et al. (2018), with data fitted to an exponential distribution (B. Keller, pers. comm., 2020; see worked example in Fig. S1).

Results

Glass chemistry

Average tuff and pumice glass compositions indicate that source magmas were peralkaline rhyolites (KBS/H2, Chari/L) and rhyodacites (Malbe/H4, Gele) (Table S3). Compositional data obtained from individual tuff and pumice glasses support attribution of pumice samples to the host KBS (=H2), Malbe (=H4) Tuff, Chari (=L) or Gele tuffs. (Fig. 3, Table S3*)*. The KBS/H2, Chari/L and Gele samples are all characterised by restricted compositional variations (Table S3), with only minor differences between individual pumice samples from respective tuffs (e.g. slightly elevated TiO_2 in Gele sample TB17-021-P2; Fig. 3). In contrast, the Malbe/H4 tuff and pumice glass compositions span a much broader compositional range (Fig. 3). Glasses from individual Malbe/H4 pumice clasts exhibit distinct compositional arrays compared to the host tuff, with the latter data spanning the entire pumice compositional range (Fig. 3). Brown et al. (2008) identified two compositional 'modes' for the Malbe Tuff, whereas current results indicate a continuum of compositions.

Feldspar chemistry

Feldspar compositions for the KBS/H2 tuff samples define a narrow range ($Or_{0.34}$ – $Or_{0.39}$) and plot close to the anorthoclase/sanidine boundary (Fig. 4). Two feldspar crystals from sample 7822-38 have more sodic compositions, but still plot within the anorthoclase field (Fig. 4). These two grains also show minor core to rim zonation, with the rims exhibiting marginally higher Ca/K ratios. Overall, the restricted range in feldspar compositions mirrors that observed for the KBS/H2 glass compositions.

Feldspar compositions from the Malbe/H4 tuff pumice samples define an even narrower range ($Or_{0.34}$ – $Or_{0.38}$) and plot adjacent to the anorthoclase-sanidine boundary, mostly within the anorthoclase field (Fig. 4). However, there are subtle variations between samples, with TB17-022-P1 feldspars exhibiting slightly higher Ca contents and F107-P1 feldspars displaying lower Ca contents. In this case the limited feldspar compositional range contrasts sharply with the wide range in tuff and pumice glass compositions.

Compared to the KBS/H2 and Malbe/H4 samples, the Chari/Tuff L and Gele feldspars from individual pumice clasts display far more compositional variability (Fig. 4). These samples show distinct compositional trends that are near-continuous for most data $\geq An_{0.07}$, with a few Gele feldspars plotting at significantly higher anorthite contents (up to $An_{0.23}$), extending into the plagioclase field (Fig. 4). In addition, a number of Gele feldspars plot in the sanidine compositional field.

The majority of feldspar samples from the KBS/H2 and Malbe/H4 samples contain low Ba contents (BaO < 0.05 wt%), with no discernible zonation patterns (Table S4). In contrast, the Chari/Tuff L and Gele feldspars are characterised by BaO concentrations ranging from 0.07 – 0.81 wt% and 0.10 – 0.85 wt%, respectively, with average values of 0.27 – 0.34 wt% and 0.37 – 0.40 wt%, respectively (Fig. S2, Table S4). Elevated Ba contents correlate with higher Na_2O/K_2O (Fig. S2) and Ca/K ratios (Table S4). Core-rim analyses of these feldspars reveal some variation within individual fragments, but 73% of Chari/Tuff L grains show no variation in Ca/K ratios, and 61% also show no variation in Ba-content (Table S4). The remaining Chari/Tuff L grains exhibit discernible core to rim zonation, but no consistent zonation patterns – for example, similar proportions of grains show elevated Ca/K and Ba in cores versus rims. By comparison, only 16% of the Gele feldspars are unzoned with respect to Ca/K values and 44% show no change in Ba content. Again there are no distinct patterns to the zonation (Table S4). The variations in Ba are highlighted in line-scan analyses completed for three feldspar crystals from Chari sample 81-219 and two from sample Tuff L-P1, plus a random grain from Tuff L-P1 showing no variation (Fig. S3).

$^{40}Ar/^{39}Ar$ Geochronology

Data from $^{40}Ar/^{39}Ar$ analyses conducted on individual pumice feldspar crystals from the KBS (=H2), Malbe (=H4), Chari (=L) and Gele tuffs are tabulated in Tables S5 and S6 and illustrated in figures 5 and 6. Estimated eruption ages were calculated using the statistical approaches outlined above and are summarised in Table 1. As noted in previous studies of tuff feldspars (e.g. Chen et al. 1996), the data define wedge-shaped patterns in inverse isochron space (Fig. S4).

KBS (=H2) Tuff

$^{40}Ar/^{39}Ar$ data were obtained from a total of 108 anorthoclase feldspar crystals from five KBS/H2 samples (7822-47A/B, 7822-38, 7722-107, TB17-009-P1, TB17-009-P2, F102-P) (Tables S5, S6; Fig. 5). Step-heating results from several individual feldspar crystals representing three KBS samples (7822-47A, 7822-38, 7722-107) show no discernible evidence of argon loss or gain (Table S5). All sample datasets exhibit positively skewed age distributions with a 'tail' towards older ages and a total range of 1872.6 ± 8.4 ka (2σ) to 1899.1 ± 1.8 ka (2σ), spanning 36.7 kyr (Fig. 5).

Eruption age estimates for the KBS/H2 samples are tabulated in Table 1. In the case of sample TB17-009-P2, ages determined using the Model 1 and 2 methods are based on only one or two datapoints. Consequently, ages were also estimated by excluding the youngest age for this sample. Overall, the nMAD method gives the oldest or equal oldest numerical ages, with the Bayesian estimation approach typically yielding the youngest ages (Table 1; Fig. 5). For five datasets (7822-47B, 7822-38, 7722-107, TB17-009-P2, F102-P), ages from the various methods are within uncertainty (Table 1). The remaining two datasets show more discordant results, although all age estimates are within 5 ka of one another (Fig. 5).

Weighted mean ages calculated for the seven KBS/H2 samples are reasonably consistent across all methods and range from 1878.9 ± 1.1 ka (2σ; MSWD = 2.3; Bayesian method; n = 7) to 1881.2 ± 1.9 ka (2σ; MSWD = 5.1; nMAD method; n = 7), a difference of 2.3 kyr (Table 1). The precision of the weighted mean Bayesian age estimate improves to 1879.1 ± 0.6 ka (2σ; MSWD = 1.3; p = 0.23) if the youngest age from sample 7822-47A is omitted (Table 1).

As the J-value calculation is a minor contributor to feldspar age uncertainties, we also calculated ages for the combined dataset (Fig 6); noting that this is not a strictly hierarchal approach to uncertainty estimation (e.g. Renne et al. 2001). The resulting composite age estimates for all methods are indistinguishable from the weighted mean values and are insensitive to the inclusion or exclusion of J-value uncertainties associated with individual analyses. For example, the composite Bayesian age estimate of 1879.1 ± 0.6 ka is identical to the weighted mean value above (Table 1).

The KBS feldspar grains have $^{40}Ar/^{39}Ar$ derived Ca/K values of 0.00762 ± 0.00034 to 0.02068 ± 0.00004 (~$An_{0.2–0.7}$). Notably, there is no obvious correlation between Ca/K values and apparent ages (Fig. 7).

Malbe (=H4) Tuff

Single feldspar crystals (n = 76) from five Malbe/H4 Tuff samples yield ages ranging from 1835.2 ± 2.0 to 1902.5 ± 2.4 ka (2σ) (Fig. 5, Tables S5, S6), spanning 71.7 kyr. If the two oldest ages (samples TB17-022-P2, 81-201) are excluded from consideration, the 'maximum' age decreases to 1865.7 ± 1.8 Ma, for a range of 34.3 kyr, analogous to that of the KBS/H2 samples.

Age estimates calculated using the five statistical approaches are summarised in Table 1. Feldspars from two samples (TB17-022-P1, F107-P1) show concordant results for all methods. For the remaining samples (TB17-022-P2, TB17-022-P3, 81-201), the nMAD method gives distinctly older age estimates, with Model 3 also yielding older ages for two samples (TB17-022-P3, 81-201). The remaining methods (Models 1/2, Bayesian) give younger, more consistent ages taking into account the uncertainties. Overall, age estimates vary from 1845.8 ± 1.5 ka (TB17-022-P2; nMAD) to 1835.7 ± 2.1 ka (TB17-022-P3; Bayesian method), a range of 13.7 ka (Table 1).

Weighted mean ages calculated for the five Malbe/H4 samples extend from 1843.1 ± 3.8 ka (MSWD = 19; nMAD method) to 1837.1 ± 0.9 ka (MSWD = 1.4; Bayesian method). The Bayesian approach produces the most concordant age estimates of 1837.4 ± 0.9 ka (MSWD = 2.3; p = 0.06; excluding older outliers) or 1837.7 ± 0.9 ka (MSWD = 1.5; p = 0.19; excluding older outliers and youngest age), with the remaining methods characterized by low probability of fit parameters ($p < 0.01$) (Table 1).

As with the KBS/H2 data, we calculated ages for the composite dataset, noting the general concordance of results with the inter-sample weighted mean determinations (Fig. 6, Table 1). At this juncture, we define a 'continuum' group of ages (including individual results within 2.5σ of adjacent datapoints), as this group shows an improved exponential distribution fit (Fig. 6). For the Malbe/H4 samples, the 'continuum' includes all but the three oldest ages. The Bayesian age estimate for the full dataset is 1836.9 ± 1.0 ka (n = 76), regardless of the inclusion/exclusion of J-value uncertainties for individual datapoints, within uncertainty of the 'continuum' group value of 1837.2 ± 0.9 ka (n = 73), indicating the insensitivity of the Bayesian algorithm to older outliers (Table 1).

The Malbe/H4 feldspar grains have $^{40}Ar/^{39}Ar$ derived Ca/K values of 0.00517 ±0.00034 to 0.07089 ±0.00034 (~$An_{0.2–2.1}$). In accord with the KBS/H2 results, there is no obvious correlation between Malbe/H4 Ca/K values and apparent ages (Fig 7).

Chari (=L) Tuff

Chari Tuff and Tuff L feldspars from five samples show strongly positively skewed apparent age distributions (Figs. 5, 6). If all data are aggregated (n = 114), ages range from 1347.3 ± 5.6 to 1949.4 ± 4.0 ka (2σ), an overall timespan of 611.7 kyr (Table S5). If ages older than the 'continuum' group are excluded (n = 17), the 'maximum' age becomes 1436.9 ± 1.6 ka, a span of 85.6 kyr (Table S5).

Quantile-Quantile plots (Fig. S4) and other tests of normality show that data in the Chari/Tuff L age continua (i.e. excluding older outliers) are not normally distributed, such that calculation of weighted mean or median absolute deviation values is inappropriate. This is clearly evident from Table 1, where calculation of nMAD and Model 1-3 ages require the exclusion of a majority of datapoints, yielding discordant weighted mean ages with low probabilities of fit (<0.01). In contrast, the Bayesian age estimates for the six datasets (all datapoints) have more limited dispersion, ranging from 1351.3 ± 6.3 ka (K82-787b) to 1364.7 ± 4.2 ka (81-219) (Table 1). The continuum datasets show slightly more precise age estimates of 1351.9 ± 6.3 ka (K82-787b) to 1364.1 ± 2.8 ka (81-219), for a weighted mean age of 1359.3 ± 3.8 ka (MSWD = 3.8; p = 0.00). If the oldest age estimate from sample 81-219 is omitted, a more precise weighted mean age of 1357.5 ± 1.8 ka (MSWD = 0.9; p = 0.45) is calculated.

The Bayesian age estimate for the combined dataset is 1356.5 ± 1.7 ka (n = 113; excluding the youngest age from K82-787b) and 1357.1 ± 1.7 ka for the continuum age array (n = 96) (Table 1). As with the KBS/H2 and Malbe/H4 samples, these values are indistinguishable from the inter-sample weighted mean age estimates calculated above (Table 1).

The majority of the age continuum grains from the Chari/Tuff L samples have Ca/K values less than 0.05 (~$An_{1.7}$), with values for the remaining grains ranging up to 0.18 (~An_5; Fig. 7). Feldspar fragments forming the older 'tail' of the age distribution have Ca/K values of 0.014 ± 0.002 to 0.873 ±0.004 (~$An_{0.5–13.2}$), and there is a discernible positive correlation between Ca/K values and apparent ages (Fig. 7, Fig. S4).

Gele Tuff

Feldspars from the Gele pumice clasts show a similar positively skewed age distribution to the Chari/L samples. Overall, apparent ages (n = 48) range from 1306.9 ± 5.2 ka

(sample TB17-021-P1) to 1570 ± 11 ka (sample TB17-021-P2), a range of 279.3 kyr (Table S5; Figs. 5, 6). The continuum age array (n = 41) has a maximum age of 1389.2 ± 6.0 ka (sample TB17-021-P2), giving a reduced age difference of 93.5 kyr.

As per the Chari/L data, the Gele age continuum data are not normally distributed (Fig. S5), thus complicating the calculation of weighted mean or median absolute deviation age estimates. This is again evident from small number of datapoints included in age estimates and the low probabilities of fit (<0.01) for most methods (Table 1).

Bayesian age estimates for the three Gele samples vary from 1309.0 ± 6.0 ka (TB17-021-P1) to 1316.8 ± 9.9 ka (TB17-021-P3). Consideration of 'continuum' datapoints only, gives age estimates of 1310.0 ± 5.6 ka to 1317.6 ± 8.2 ka (Table 1). Weighted mean ages for the three samples are 1314.9 ± 2.3 ka (MSWD = 1.9; p = 0.15; n = 3) for the continuum array and 1315.4 ± 1.9 ka (MSWD = 0.3; p = 0.75) if the youngest age from sample TB-021-P1 is excluded (Table 1).

The composite dataset has a Bayesian age estimate of 1315.4 ± 2.4 ka (n = 47) or 1315.4 ± 2.0 ka (n = 40) for the continuum age group, excluding the youngest datapoint (Fig. 6). As noted for previous tuffs, these values are unaffected by the inclusion or exclusion of J-value uncertainties and are indistinguishable from the weighted mean age estimates.

The Gele continuum feldspars have Ca/K values of 0.0476 ± 0.0006 to 0.483 ± 0.004 (~$An_{1.7–11.0}$), whereas the grains in the older 'tail' have Ca/K values of 0.165 ±0.001 to 1.208 ±0.002 (~$An_{4.7–15.0}$) (Fig. 7). As observed for the Chari/Tuff L samples, there is a discernible correlation between Ca/K values and apparent ages (Fig 7).

Discussion

Causes of older $^{40}Ar/^{39}Ar$ ages and insights into eruption dynamics

Feldspar crystals from the KBS/H2, Malbe/H4, Chari/Tuff L and Gele tuff samples all show $^{40}Ar/^{39}Ar$ age variability beyond that attributable to analytical or reactor related uncertainties (Figs 5, 6). Similar dispersion has been observed in other silicic volcanic rocks, where feldspar $^{40}Ar/^{39}Ar$ age arrays typically define broadly exponential distributions (e.g. Andersen et al. 2017; van Zalinge et al. 2022). The older ages in these arrays are usually attributed to excess argon contamination and/or the presence of

antecrysts/xenocrysts (Schaen et al. 2020 and references therein). In contrast, younger ages are typically considered to be caused by argon loss, irradiation artefacts (e.g. fluence gradients, self-shielding) or analytical bias (e.g. blank aberrations, hydrocarbon interferences) (Schaen et al. 2020 and references therein).

Of the four Turkana Basin tuffs, the KBS/H2 and Malbe/H4 tuff samples are characterised by broadly similar $^{40}Ar/^{39}Ar$ age distributions with restricted age ranges (37 - 78 kyr, respectively), narrow feldspar compositional fields (Fig. 4) and no obvious correlation between feldspar ages and composition (e.g. Ca/K ratios; Fig. 7). In contrast, the Chari and Gele feldspar samples embody age ranges >250 ka (Figs. 5, 6), broader feldspar compositional variations (Fig. 4) and distinct correlations between age and Ca/K ratios (Fig. 7). The latter correlations suggest that the older $^{40}Ar/^{39}Ar$ ages are more likely due to the retention of inherited (i.e. pre-eruption) radiogenic argon rather than excess argon contamination, as the latter is unlikely to be related to compositional trends. This interpretation is supported by recent studies of silicic volcanic systems showing consistent U-Series/U-Pb zircon and $^{40}Ar/^{39}Ar$ feldspar ages, indicating 'cold storage' of crystal accumulations for periods up to several million years (van Zalinge et al. 2022; Cooper and Kent 2014). Modelling of radiogenic argon accumulation and diffusional loss rates in crystal reservoirs indicates that feldspar crystals must be stored below ~475˚C to retain inherited argon (Andersen et al. 2017; van Zalinge et al. 2022). In addition, magma residence times prior to eruption must be short (years to 10's of years) in order to preserve older $^{40}Ar/^{39}Ar$ ages during exposure to elevated liquidus temperatures (>750˚C) (van Zalinge et al. 2022). The less than perfect relationship between age and composition in the Turkana tuff samples is probably a function of local magma temperatures, time of exposure of crystals to the magma prior to eruption and the diffusivity characteristics of individual feldspar crystals; although we cannot totally discount the possible presence of excess argon (e.g. from glass inclusions).

The above scenario accords with current understanding of the dynamics of large silicic magmatic systems (e.g. Cooper and Kent, 2014; Cashman et al. 2017; van Zalinge et al. 2022), which are viewed as a series of crustal-scale reservoirs dominated by crystal mush and crystal accumulations, stored at temperatures ranging from liquidus values to below ~450 ˚C (Cooper and Kent 2014; van Zalinge et al. 2022). The limited volumes of melt associated with these reservoirs also accounts for the lack of geophysical evidence for large melt accumulations associated with silicic systems (e.g. Hübert et al. 2018). Intrusions of mafic magmas are thought to produce periodic silicic

magma hot zones in the upper crust that occasionally erupt explosively (Sparks et al. 2019; Cashman et al. 2017).

The current combination of $^{40}Ar/^{39}Ar$ and glass/feldspar compositional data provide new insights into the eruption dynamics of the source volcanic systems that produced the Turkana tuffs. The restricted age and chemistry of the KBS/H2 samples (Figs. 4, 6) implies the eruption of a homogenous, more evolved rhyolitic magma with very limited inclusion of older antecrysts. The variable glass chemistry of the Malbe/H4 samples (Figs. 4, 6) suggests a more heterogeneous evolved rhyodacite magma, possibly caused by the mixing of magmas with slightly different compositions. The tight clustering of feldspar compositions is again consistent with limited entrainment of older antecrysts (or xenocrysts).

The elevated Ba contents of the Chari/Tuff L and Gele feldspars (Table S4) indicates that their source magmas were less evolved than those that produced the KBS/H2 and Malbe/H4 tuffs, as Ba partitions preferentially into early feldspar crystals (e.g. Iddon et al. 2019). The distinct feldspar major element arrays defined by the Chari/L and Gele feldspars (Fig. 4) imply continuous fractional crystallisation trends. However, the higher, more variable Ba contents associated with the sodic feldspars (Figs. S1, S2) indicate a more complex scenario, with these grains likely to be antecrysts. This accords with similar feldspar chemistries observed in younger peralkaline rhyolitic volcanics from the Main Ethiopian Rift (MER) (Iddon et al. 2019). The Chari/Tuff L and Gele eruptions appear to have been generated from relatively homogenous melts that entrained juvenile as well as older, antecrystic feldspar crystals. Broadly similar eruption models have been proposed for the Bishop Tuff (Andersen et al. 2017) and Central Andes volcanics (van Zalinge et al. 2022), suggesting that such eruption dynamics are more typical of silicic magma systems than previously envisaged.

Comparison of eruption age estimation methods

It is generally accepted that tuff eruption ages are best represented by the youngest sub-set of concordant feldspar ages that are unaffected by inherited argon, excess argon, argon loss or other irradiation/analytical biases leading to anomalous ages (Schaen et al. 2020 and references therein). However, there is limited agreement on the best approach(es) for constraining these ages. Differences in eruption age estimates from the five statistical methods trialled in this study are relatively minor (~ 2 ka) for the

KBS (=H2) Tuff, which is characterised by the smallest age range and a near-normal age distribution, but are more significant (6 – 9 ka) for the Malbe/H4, Chari/Tuff L and Gele feldspar samples, which exhibit non-normal distributions (Table 1).

Of the statistical approaches employed, the normalized median absolute deviation method (nMAD) typically produced the oldest age estimates, followed by the 'normality test and goodness-of-fit filter' method (Model 3) (Table 1, Fig. 8). This is not entirely unexpected, as the nMAD/'gap' outlier exclusion approach essentially forces a normal distribution by excluding both older and younger ages (e.g. Deino et al. 2019). Given the distinctly non-gaussian distributions of the current datasets (in particular the Chari/Tuff L and Gele samples), this method typically yields the most discordant intra-sample age results and is thus non-ideal for such dispersed age distributions. The 'normality test and goodness-of-fit filter method' (Model 3) also yields older eruption age estimates in most cases, as it is based on the largest array of datapoints that define a normal distribution and meet goodness of fit parameters (e.g. $p > 0.05$; see Schaen et al. 2020). This method produced the least consistent intra-sample results and may be better suited to larger datasets. The low MSWD weighted mean (Model 1) and weighted mean filter (Model 2) methods invariably give younger age estimates that should equate with eruption events if the data are minimally affected by argon loss or other irradiation/analytical artefacts that would cause anomalously young ages. However, these methods again show poor inter-sample age consistency for the Turkana tuffs, with younger ages tending to be associated with larger sample sizes (Schaen et al. 2020).

In contrast to the aforementioned approaches, the Bayesian estimation approach minimises the need for older outlier identification, removing some subjectivity. The insensitivity of the approach to older outliers is illustrated by the equivalence of ages determined for all datapoints compared to those calculated from the continuum datasets (Table 1). However, the Bayesian algorithm is associated with the youngest eruption age estimates for most samples and shows some sensitivity to young outliers. Nonetheless, the Bayesian method shows the most consistent inter-sample ages per locality, with concordance further enhanced for the KBS/H2 and Gele tuff samples by omitting just two anomalously young datapoints (KBS sample 7822-47A and Gele sample TB17-021-P1) (Table 1). The exclusion of additional young datapoints has minimal impact on the ages, suggesting that the two (anomalously young) KBS/Gele grains may be affected by argon loss and/or irradiation/analytical aberrations.

Despite the advantages of a stochastic age estimation approach, the possibility of age bias towards younger ages due to argon loss related issues cannot be ignored. We attempted to mitigate this issue through the careful selection of optically clear feldspar fragments devoid of obvious alteration, combined with evidence from EPMA data and available (albeit limited) step-heating results, which show no evidence of alteration or argon loss, respectively. In addition, the concordance of inter-sample Bayesian age estimates suggests that argon loss is not a major factor. Nevertheless further work is required to test the Bayesian approach more rigorously for age robustness.

Eruption age estimates and comparisons to previous studies

KBS (=H2) Tuff

As noted above, similar eruption age estimates were obtained for the KBS/H2 feldspar samples from all statistical approaches. However, as the Bayesian age estimates are the most concordant across all samples, our preferred age for the KBS (=H2) Tuff is 1878.9 ± 1.1 ka (MSWD = 2.3; p = 0.03) or 1879.1 ± 0.6 ka (MSWD = 0.61; p = 0.31) if the youngest age (sample 7822-47A) is excluded from consideration. The inclusion of external uncertainties increases the above values to ± 2.6 ka and ± 2.4 ka, respectively (Table 1). Our preferred age for the KBS (=H2) Tuff (1879.1 ± 0.6/2.4 ka) is within uncertainty of previous bulk K-Ar, $^{40}Ar/^{39}Ar$ and fission track ages (Table 1), apart from the considerably older values reported by Fitch and Miller (1970), Fitch et al. (1976), Hurford et al. (1976) and Fitch et al. (1996) (Fig. 2, Table S1). This result is also indistinguishable from the weighted mean $^{40}Ar/^{39}Ar$ age of 1873 ± 28 ka obtained from single-feldspar analyses by McDougall and Brown (2006), despite the use of different statistical approaches. In this case, the similarity is attributable to the restricted age range of the KBS/H2 dataset (Fig. 6).

The $^{40}Ar/^{39}Ar$ age of the Turoha Tuff (TRT) in the Konso Formation (1960 ± 60 ka; Katoh et al. 2000) is within uncertainty of the KBS age reported by McDougall and Brown (2006), but is distinctly older than the current eruption age estimate (1879.1 ± 0.6 ka). Nonetheless, the youngest individual TRT feldspar ages (e.g. 1878 ± 80 ka; 2σ) are within uncertainty, raising the possibility that, if equivalent, the Turoha Tuff may contain a higher proportion of older feldspar antecrysts. Although Brown et al. (2006) question the correlation with the KBS Tuff based on glass geochemistry differences, the age and geochemistry of the TRT are not sufficiently dissimilar to rule

out a correlation with the KBS/H2 Tuff and further geochronology and geochemistry are warranted to test this correlation.

Malbe (=H4) Tuff

The Bayesian approach again gives the most concordant age estimates for the Malbe/H4 samples and our preferred ages are 1837.4 ± 0.9 (± 2.4 ka; MSWD = 2.3; p = 0.06) or 1837.7 ± 0.9 (± 2.4 ka; MSWD = 1.5; p = 0.19), excluding the youngest age (full external uncertainties are shown in brackets) (Table 1). These values are within uncertainty of the K-Ar (1850 ± 40 ka) and $^{40}Ar/^{39}Ar$ (1850 ± 12 ka) ages reported by McDougall (1985) and McDougall and Brown (2006), respectively, but slightly older than earlier K-Ar ages of Drake et al. (1980) and McDougall et al. (1980) (Table S1).

Our study reveals that the eruptions of the KBS and Malbe tuffs were separated by some 40 – 43 kyr, where the previous chronology was indistinguishable (McDougall and Brown, 2006) (Fig. 6, Table S1). The Malbe/H4 Tuff overlies the KBS/H2 Tuff by ~16 m in the Shungura Formation (Cerling and Brown 1982) and ~15 m in the Koobi Fora Formation (Feibel 1983; McDougall and Brown 2006), indicating local sedimentation rates of ~39.7 and ~37.3 cm/kyr, respectively for the interval between the two tuffs. These values provide useful constraints for interpolating fossil ages in adjacent sediments.

Chari (=L) Tuff

The age of the Chari (=L) Tuff is less well constrained than the other tuffs owing to its large age dispersion and lower precision on individual $^{40}Ar/^{39}Ar$ analyses, caused by smaller feldspar grain sizes and lower potassium contents for many grains (Table S5). In addition, the Chari/Tuff L samples yield a less robust discordant Bayesian weighted mean age estimate (1359.3 ± 3.8/4.2 ka; MSWD = 3.8; p = 0.00), with the age estimate for sample 81-219 being distinctly older than those from the remaining five datasets, possibly due to greater retention of inherited argon. Omission of this sample from the weighted mean calculation gives a more robust result of 1357.5 ± 1.8 ka (± 2.5 ka; MSWD = 0.9; p = 0.45), which is our preferred age for the Chari (=L) Tuff.

This age is within uncertainty of previous (imprecise) K-Ar ages for the Chari Tuff (Fig. 2, Table S1), but is distinctly younger than the weighted mean age of 1386 ± 10 ka reported by McDougall and Brown (2006). This discrepancy is attributed to the different statistical approach adopted in the earlier study. Application of the Bayesian

algorithm to the McDougall and Brown (2006) $^{40}Ar/^{39}Ar$ results gives a weighted mean age estimate of 1359.2 ± 7.5 ka (MSWD = 1.9), indistinguishable from current results (Fig. 9).

The Chari (=L) Tuff and Bright White Tuff (BWT) in the Konso Formation have similar tuff glass chemistries (Katoh et al. 2000), but the reported BWT age of 1440 ± 40 ka is notably older than current and earlier Chari/Tuff L (McDougall and Brown 2006) determinations (Table S1). As was the case for the TRT, the youngest BWT age of 1375 ± 80 ka is within uncertainty of the Chari/L ages, supporting correlation of the tuffs.

Gele Tuff

The more consistent Bayesian weighted mean age estimates for the three Gele Tuff samples are preferred here: 1314.9 ± 2.3 ka (± 2.8 ka; MSWD = 1.9; p = 0.15) or 1315.4 ± 1.9 ka (± 2.5 ka; MSWD = 0.3; p = 0.75) if the youngest age from sample TB-021-P1 is excluded (Table 1). These ages are indistinguishable from an early, imprecise K-Ar age of 1250 ± 60 ka (Brown et al. 1985), but younger than the weighted mean $^{40}Ar/^{39}Ar$ age (1331 ± 8 ka) reported by McDougall and Brown (2006) (Table 1, Fig. 2, Table S1). As above, application of the Bayesian approach to the latter data gives a younger, analogous age (1307 ± 9 ka). The Gele and Chari Tuffs do not crop out in the same sections and current results confirm their relative stratigraphic positions.

Anchoring paleoclimate proxy data

Uncertainties in the current tuff ages (±2-3 ka) are less than, or similar to, those typically assigned to astronomically tuned, deep-sea core sequences (±2-5 ka; e.g. Channell et al. 2020). As a result, the tuffs provide unambiguous anchor points for astronomical tuning of adjacent sedimentary units and facilitate the testing of terrestrial paleoclimate and paleoenvironmental models. In turn, astronomically tuned sedimentary sequences have the potential to provide improved interpolation of fossil ages, compared to estimates based on bracketing tuff and geomagnetic time markers or (often highly variable) sedimentation rates (Joordens et al. 2011, 2013).

Studies aimed at reconstructing paleoclimate records for Turkana Basin sediments have utilised either low resolution sequence stratigraphy (e.g. Lepre et al. 2007; Nutz et al. 2017) or millennial timescale geochemical proxy records such as hydrogen plus

carbon isotopic measurements of leaf waxes (Lupien et al. 2018, 2020) and $^{87}Sr/^{86}Sr$ isotopic data from marine fossils (Joordens et al. 2011, 2013). Leaf wax records were acquired from paleolake sediments in drill-core WTK13 (see Campisano et al. 2017), located on the northwest margin of Lake Turkana by Lupien et al. (2018, 2020). The upper section of core material includes the Chari, Etirr and Ebei tuffs as well as an unnamed tuff spanning an interval from ~1370 to 1500 ka. However, this interval also has the lowest density of δD_{wax} and δC_{wax} isotopic data, which hinders tuning of these proxy records (Lupien et al. 2018). In contrast, a more continuous marine fossil $^{87}Sr/^{86}Sr$ isotope record is available for the Upper Burgi Member (UBM), immediately below the KBS (=H2) Tuff, extending beyond the base of the Olduvai subchron (bC2n) and possibly including a short (normal polarity) excursion thought to be the Pre-Olduvai event in Area 131 (Joordens et al. 2011, 2013).

$^{87}Sr/^{86}Sr$ data for fish fossils recovered from paleo-lake sediments (Lake Lorenyang phase) below the KBS Tuff in the UBM of the Koobi Fora Formation (Fig. 10) have been interpreted to reflect orbitally modulated paleoclimate (~21 ka precession) cycles (Joordens et al. 2011, 2013), driven by fluctuating Mediterranean monsoonal intensity (e.g. deMenocal 1995; Potts 2013). The Sr isotope paleoclimate proxy is based on the premise (i.e. unsupported by analyses) that the paleo-Omo River in the north drained low $^{87}Sr/^{86}Sr$ (~0.704) volcanic rocks of the Ethiopian Highlands, whereas the paleo- Kerio and Turkwel rivers to the south drained metamorphic terranes characterized by higher $^{87}Sr/^{86}Sr$ isotopic values >0.720 (Joordens et al. 2011, 2013). Accordingly, monsoonal maxima (wet periods) that increased drainage from the paleo-Omo River are considered to have lowered $^{87}Sr/^{86}Sr$ ratios in the lake, whereas periods of reduced monsoonal strength (dry periods) led to increased lake $^{87}Sr/^{86}Sr$ (Joordens et al. 2011, 2013; cf. van der Lubbe et al. 2017). In an initial study Joordens et al. (2011) tuned the UBM Sr isotopic record relative to an age of 1945 ± 4 ka (Lourens et al. 2004) for the base of the Olduvai geomagnetic Subchron (bC2n). However, astronomical age estimates for the bC2n excursion are contentious and vary by ~43 ka (Shackleton et al. 1990; Lourens et al. 2004; Lisiecki and Ramo 2005; Channell et al. 2020), or approximately two precession cycles, thus limiting the utility of bC2n as an anchor for orbital tuning models.

The new, astronomically calibrated KBS Tuff age represents a more robust anchor point for testing available UBM tuning models and, hence, the utility of the Sr isotope

proxy approach (Fig. 10). A revised tuning model (Model I) for the sedimentary section below the KBS Tuff in the Upper Burgi Member (Areas 102, 105; Koobi Fora Formation) was constructed using published $^{87}Sr/^{86}Sr$ isotopic data from marine fossils (Joordens et al. 2011, 2013), available stratigraphic logs (Joordens et al. 2011, 2013), the 65^{o}N summer insolation model of the La2004 (Laskar et al. 2004) astronomical solution, and the astronomically calibrated KBS Tuff age of 1879.1 ± 2.4 Ma (Table 1). As per previous work (Joordens et al. 2011, 2013), we assumed variable sedimentation rates across the section and initially tuned maximum Sr isotopic values to insolation minima (i.e. drier cycles) and minimum Sr isotopic values to insolation maxima (i.e. wetter cycles) (Model I) (Table S7). This tuning option is similar to Model 4 of Joordens et al. (2011). In the case of Model II, we tuned maximum Sr isotopic values to insolation minima above the more sandy units in the UBM section (Fig. 10) relative to the above KBS age, and to insolation maxima below the sandy units relative to an age of 1968 ± 2 ka for bC2n (Lisiecki and Ramo 2005) (Fig. 10; Table S7).

Our revised tuning Model I, calibrated to the KBS Tuff, includes six precession cycles that align with sapropel (Lourens et al. 1996) and dust records (Tiedemann et al. 1994) for Mediterranean and Atlantic Ocean ODP sites (Fig. 10). The alignment of the KBS Tuff on the younger side of an insolation minimum ($^{87}Sr/^{86}Sr$ maximum) is consistent with model assumptions (Joordens et al. 2011) (Fig. 10). However, the bC2n excursion aligns with an insolation minimum (Fig. 10), rather than the insolation maximum inferred from marine records (Lisiecki and Ramo 2005; Channell et al. 2020). In this case, the tuned ages of the bC2n and older Pre-Olduvai geomagnetic transitions are 1975 ± 2 ka and >1997 ka (Fig. 9), distinctly older than previous estimates of 1925 – 1968 ka and ~1977 ka, respectively (see Channell et al. 2020 and references therein). Furthermore, Model I contrasts with the $^{87}Sr/^{86}Sr$ record for Lake Turkana during Holocene times, where elevated $^{87}Sr/^{86}Sr$ ratios correlate with an insolation maximum (van der Lubbe et al. 2017). These inconsistencies cast doubt on the underlying assumptions of the UBM $^{87}Sr/^{86}Sr$ isotope proxy tuning models. Possible reasons for this include: i) incorrect assignment of $^{87}Sr/^{86}Sr$ ratios to the paleo-Omo versus paleo- Kerio and Turkwel rivers – for example modern $^{87}Sr/^{86}Sr$ values for these drainages are all analogous (T. Cerling pers comm. in van der Lubbe et al. 2017); ii) a non-continuous paleoclimate proxy record in the UBM sediments, owing to the influence of local drainages and/or the reworking of sediments and fish fossils, and iii) fluctuations in local and/or regional hydrodynamic patterns related to changing

paleoclimate factors, such as E-W migration of the Intertropical Convergence Zone (ITCZ) and the onset of Pacific Walker circulation at ~2.0-2.2 Ma (van der Lubbe et al. 2017, 2021).

It is possible to reconcile the above inconsistencies by constricting the $^{87}Sr/^{86}Sr$ cycles by a half precession cycle (i.e. ~10.5 ka) in the middle of the UBM succession (Model II) (Fig. 10). It is notable that this part of the stratigraphy is dominated by slightly coarser sandy units, rather than lacustrine silts (Fig. 10), and coincides with a step-change in average $^{87}Sr/^{86}Sr$ ratios (Fig. 10). Although possible triggers for the shift are unclear, this period (~1.85 – 1.9 Ma) was characterised by increasing lake levels, the volcanic closure of drainage outlets to the Indian Ocean (1.8 – 2.2 Ma) (Boes et al. 2018 and references therein) and changing paleoclimate patterns (van der Lubbe et al. 2017, 2021). Assuming that the sand units reflect a change in hydrodynamic regime, we constructed a revised tuning model (Model II, Fig. 10), with the younger record tuned to the KBS tuff age and the older record tuned to a bC2n age of 1968 ± 2 ka (Lisiecki and Ramo 2005) (Table S7). The latter age is preferred, as younger age estimates for bC2n (1925 and 1945 ka; Channell et al. 2020; Horng et al. 2002) are incompatible with the number of definable Sr cycles and would invalidate the $^{87}Sr/^{86}Sr$ proxy assumptions. While speculative, this tuning model is consistent with ages for the KBS Tuff and bC2n (tuned age = 1965 ± 3 ka) and maintains alignment with Mediterranean sapropel (Lourens et al. 1996) and Atlantic Ocean dust (Tiedemann et al. 1994) records (Fig. 10). Nonetheless, further testing of the $^{87}Sr/^{86}Sr$ paleoclimate proxy approach is clearly warranted. Our modelling demonstrates the particular challenge in tuning terrestrial paleoclimate proxy records and highlights the importance of robust tuff (and geomagnetic excursion) ages for anchoring terrestrial tuning models in the Turkana Basin and other terrestrial settings.

Hominin fossil ages

Temporal constraints on hominin fossils recovered from Turkana Basin sediments rely on ages of bracketing tuff, geomagnetic and stratigraphic time markers, taking into account associated uncertainties (e.g. Feibel et al. 1989, 2009; McDougall and Brown 2006). Where stratigraphic logs indicate more or less continuous deposition (i.e. no significant hiatuses), hominin fossil ages have been interpolated using stratigraphic scaling (e.g. Feibel et al. 1989, 2009; Lepre and Kent 2010, 2015). Astronomically

tuned sedimentary sequences, such as the UBM (Fig. 10), have the potential to provide improved age assignment for sediment/fossil deposition (Joordens et al. 2011, 2013). However, as the Sr isotope tuning model is unproven, attribution of hominin fossil ages using this approach may be premature. The improved age precision of tuffs dated in the current study provides an opportunity to refine temporal estimates for some associated fossils, although broader revision must await high precision geochronology of additional tuffs.

Relatively few hominin fossils occur in close stratigraphic proximity to the Chari (=L) or Gele tuffs. However, well preserved early Acheulean tools occur in strata stratigraphically underlying the Bright White Tuff (BWT) in the Konso region (Beyene et al. 2013), which is correlated with the Chari Tuff. In addition, an unusual bone hand-axe was recovered from the same region, located ca.9m above the BWT and assigned an age of ~1.3 - 1.4 Ma (Sano et al. 2020). Our preferred age for the Chari/L/BWT Tuff revises the maximum age of the hand-axe to 1357.5 ± 2.5 ka. More significantly, the presence of the Chari Tuff in the WTK13 core offers robust anchoring of future high resolution paleoclimate proxy data.

The circa 1.9 Ma time period that encompasses the KBS (=H2) and Malbe (=H4) tuffs is more notable archeologically, owing to the co-existence of multiple hominin species in the region, the appearance of *Homo erectus* (*H. erectus*), increased *Homo* brain sizes, the development of Acheulean stone tools and the commencement of *Homo* dispersion beyond Africa (e.g. Leakey et al. 2012; Potts 2013; Herries et al. 2020). This period also coincided with significant environmental changes, including elevated lake levels in eastern Africa, expanded distribution of C4 vegetation and an upsurge in bovid fauna diversity (Levin 2015 and references therein). The KBS and Malbe tuffs occur in close association with Oldowan (Mode 1) stone tools (Leakey 1970) as well as several important hominin fossils, including *H. erectus* and early non-*erectus Homo* members of the '1813' and '1470' Groups (formerly *H. habilis* and *H. rudolfensis)* (Leakey 1973, 1974; Leakey et al. 2012; Anton et al. 2014).

We determined hominin fossil ages for the KBS and UBM stratigraphic sections immediately above and below the KBS and Malbe tuffs. Revised ages for hominin fossils recovered from sediments in Areas 12, 102, 105, 106, 107, 123 and 131, were determined using published stratigraphic sections (Joordens et al. 2011, 2013; Lepre and Kent 2010), a range of possible sedimentation rates, new ages for the KBS and Malbe tuffs, age estimates for the Olduvai geomagnetic transitions (tC2n, bC2n) and

distinctive stratigraphic markers (mollusc-rich C4 and A2 stromatolitic markers) (Table S8). To account for the variability in tC2n and bC2n age estimates (Channell et al. 2020), median values were calculated using the full range of available estimates (1776 ± 11 ka; 1946 ± 26 ka, respectively) (Table S8). Sedimentation rates were estimated based on lithologic composition and thickness, assuming essentially continuous sediment accumulation in designated sections. As sedimentation rates are typically highly variable, fossil age determinations are restricted to specimens recovered within ~15m of time markers (with some exceptions), where the impact of sedimentation variability is more limited. As fossils may have been reworked upwards in the sequence, these ages are essentially minimum estimates. Propagated uncertainties assigned to ages include uncertainties in the ages of the tuffs, geomagnetic and stratigraphic markers, stratigraphic position relative to chronological markers (±1 m), and the range of estimated sedimentation rates (Table S8).

The widespread C4 bio-stratigraphic marker occurs a few meters above the KBS and Malbe tuffs (Feibel et al. 1989) and is associated with a number of early hominin fossils in Area 123 (~40 km south of Area 105), including crania from the important early hominin Group 1813 (*H. habilis*) (e.g. Feibel et al. 2009). The timing of the C4 marker is constrained by its location ~13 m above the KBS Tuff in section 102-17U (Koobi Fora type section) and ~10 m above the Malbe Tuff in section 102-18 (Feibel 1983). Based on assumed sedimentation rates of 20-30 cm/ka for the KBS-C4 section, which contains few sandy units, we obtain an age of 1827 ± 11 ka for the C4 marker, comparable to a previous estimate of ~1840 ka (Feibel et al. 2009). For UBM sediments above C4, which contain thicker sandy units, we assumed sedimentation rates of 20-60 cm/ka (Table S8).

With reference to the revised C4 age of 1827 ± 11 ka, we estimated ages for Area 123 specimens located within ~15 m of the C4 marker. Ages range from 1812 ± 17 (KNM-ER1811) to 1887 ± 47 ka (KNM-ER 1502) (Fig. 11; Table S8), and are marginally younger than prior estimates (Feibel et al. 2009), with reduced uncertainties. Revised age estimates for early *Homo* (Group 1470; *H. Rudolfensis*) specimens from Area 131 (Leakey 1973; Leakey et al. 2012) range from 1899 ± 7 ka (KNM-ER 1483) to 1984 ± 27 ka (KNM-ER 62000) (Fig. 11; Table S8). Thus, Group 1813 (*H. habilis*) specimens overlap temporally with other early *Homo* species, including Group 1470 (*H. rudolfensis*) (<1.88 to ~2.06 Ma; Leakey et al. 2012; Joordens et al. 2013), reaffirming the presence of multiple early hominin species in the region at circa 1.9 Ma.

Previous age estimates for the important early *H. erectus* cranium KNM-ER 3733, the most complete example from the Koobi Fora Formation, range from ~1780 ka (Feibel et al. 1989) to ~1630 ka (Lepre and Kent 2015). Using the stratigraphic correlations of Tindall (1985), the Area 104 lithological section of Lepre and Kent (2015), a magnetostratigraphic age of 1776 ± 11 ka for the A2 marker bed (Area 104; Lepre and Kent 2015), a revised Bayesian age estimate for the Morte Tuff (1497 ± 6 ka; data from McDougall and Brown 2006) and a median age for tC2n (1776 ± 11 ka) (Fig. 11, Table S8), we calculate an age of 1591 ± 40 ka for KNM-ER 3733 (Table S8), marginally younger than prior estimates (McDougall et al. 2012; Lepre and Kent 2015). Older hominin fossil fragments attributed to early *H. erectus*, KNM-ER 2598 and KNM-ER 3228 (Leakey 1974; Wood and Leakey 2011), were recovered from normally magnetised sediments below the KBS Tuff. We obtain an age of 1915 ± 15 ka for the latter specimen, consistent with previous estimates of ~1921 ka (Leakey 1974) and 1950 ± 50 ka (Feibel et al. 1989) (Fig. 11; Table S8). A significantly older age of ~2040 to 1950 ka was reported for a *H. erectus* (DNH134) cranium from the Drimolen site in South Africa, based on (relatively imprecise) US-ESR molar ages of 2040 ± 48 ka (2σ) and 1960 ± 29 ka (2σ), a location below bC2n, and the absence of the ~2080 ka Huckleberry Ridge magnetic reversal event in underlying strata (Herries et al. 2020). If correct, DNH134 would be the oldest known occurrence of *H. erectus*. However, it is notable that the ca. 1977 ka pre-Olduvai geomagnetic excursion was not recognized in the Drimolen site (Herries et al. 2020), despite its identification in other Malapa cave deposits. Therefore, it is possible that DNH134 is located stratigraphically higher than previously thought, between bC2n and the pre-Olduvai excursion (i.e. ~1925 to 1977 ka). Nonetheless, if the Drimolen Cave magneto-stratigraphy is correct, this raises the possibility that *H. erectus* evolved in southern Africa, before dispersing northwards to eastern Africa and then Eurasia.

Conclusions

$^{40}Ar/^{39}Ar$ dating of pumice feldspar grains from KBS/H2, Malbe/H4, Chari/Tuff L and Gele tuff localities in the Turkana Basin yield variably dispersed, positively skewed age distributions. The KBS/H2 and Malbe/H4 samples are characterised by relatively restricted ranges in age (36.7 kyr and 71.7 kyr, respectively) and feldspar composition, with no relationship between feldspar ages and composition. In contrast, the Chari/Tuff

L and Gele samples display broader age ranges (>250 kyr), distinct feldspar compositional arrays and discernible correlations between feldspar ages and compositions. Consequently, the older ages are attributed to the retention of inherited argon by feldspar antecrysts/phenocrysts in response to 'cold storage' in crystal reservoirs followed by rapid melt infiltration and eruption. The combination of $^{40}Ar/^{39}Ar$ age and glass/feldspar compositional data provides insights into the longevity and dynamics of (still unidentified) source magma reservoirs.

An evaluation of statistical approaches reveals that the most concordant $^{40}Ar/^{39}Ar$ eruption ages derive from the Bayesian estimation approach. This method gives preferred, astronomically calibrated ages of 1879.1 ± 0.6 ka (± 2.4 ka including external errors) for the KBS (=H2) Tuff, 1837.4 ± 0.9 ka (±2.4 ka) for the Malbe (=H4) Tuff, 1357.5 ± 1.8 ka (±2.5 ka) for the Chari (=L) Tuff and 1315.4 ± 1.9 ka (±2.5 ka) for the Gele Tuff. With some exceptions, these ages are consistent with previous age determinations, but are more precise.

As uncertainties in the current tuff ages (±2-3 ka) and similar to those of astronomically tuned, deep-sea core sequences (±2-5 ka), the tuffs provide important anchor points for astronomical tuning of associated sedimentary sequences. Tuning of published $^{87}Sr/^{86}Sr$ proxy data from the UBM relative to the KBS Tuff age reveals some inconsistencies with geomagnetic excursions and Holocene data, suggesting complex interactions between paleoclimate and geological drivers of sedimentation.

The new age results also permit updated age estimates for important early *Homo* fossils and stratigraphic marker horizons in the KBS Member and UBM. Revised ages for Group 1813 (*H. habilis*) and Group 1470 (*H. Rudolfensis*) fossils range from 1812 ± 17 (KNM-ER 1811) to 1887 ± 47 ka (KNM-ER 1502) and from 1899 ± 7 ka (KNM-ER 1483) to 1984 ± 27 ka (KNM-ER 62000), respectively consistent with multiple early hominin species occupying the Turkana Basin at circa 1.9 Ma. Calculated ages for the important *H. erectus*, specimens, KNM-ER 3733 and KNM-ER 3228 are 1591 ± 40 ka and 1915 ± 15 ka, respectively.

The above results highlight the importance of a high resolution temporal framework for human evolution and paleoclimate/paleoenvironmental studies. Additional high-precision $^{40}Ar/^{39}Ar$ studies of Turkana Basin tuffs are needed to further test models relating paleoclimate and paleoenvironmental variations to hominin evolution and migration.

Data Availability. All data that support this study research are included in the article and/or supporting information.

ACKNOWLEDGEMENTS. This study is dedicated to the memory of Professors Ian McDougall and Frank Brown, who passed away in 2018 and 2017, respectively. This study could not have been undertaken without their encyclopedic knowledge of the Turkana Basin. Financially, the study was supported by Australian Research Council Discovery grant DP180101412 to DP, AJWG, JH, ELM, IM and ML. The Melbourne $^{40}Ar/^{39}Ar$ Laboratory receives ongoing operational support under the AuScope program of the National Collaborative Research Infrastructure Strategy. S. Szczepanski is thanked for technical assistance in the Melbourne $^{40}Ar/^{39}Ar$ laboratory. G. Hutchinson is acknowledged for assisting with the electron microprobe analyses. We also thank A. Savelkouls and H. Dalton for drafting various figures, S. Samim for assisting with sample preparation and J. Silver for generating the inverse isochron plots. The manuscript has benefitted from formal reviews by C. Hall and an anonymous reviewer.

Competing interests

To the best of their ability, the Journal has determined that Professors Brown and McDougall worked on this project and that there were no competing interests.

References

Andersen, N.L., Jicha, B.R., Singer, B.S. and Hildreth, W. 2017. Incremental heating of Bishop Tuff sanidine reveals pre-eruptive radiogenic Ar and rapid remobilization from cold magma storage. *Proceedings of the National Academy of Science,* **114**, 12407-12412.

Anton, S.C., Potts, R., Aiello, L.C. 2014. Evolution of early *Homo*: An integrated biological perspective. *Science,* **345** (6192), 123682.

Beyene, Y., Katoh, S., WoldeGabriel, G., Hart, W.K., Uto, K., Sudo, M., Kondo, M., Hyodo, M., Renne, P.R., Suwal, G. and Asfaw. B. 2013. The characteristics and chronology of the earliest Acheulean at Konso, Ethiopia. *Proceedings of the National Academy of Science,* **110(5)**, 1221285110.

Boës, X., Prat, S., Arrighi, V., Feibel, C., Haileab, B., Lewis, J. and Harmand, S. 2018. Lake-level changes and hominin occupations in the arid Turkana basin during volcanic closure of the Omo River outflows to the Indian Ocean. Quaternary Research, **91**, 892-909.

Brown, F.H. and Feibel, C.S. 1985. Stratigraphical notes on the Okote Tuff Complex at Koobi Fora, Kenya. *Nature*, **316**, 794-797.

Brown, F.H. and Feibel, C.S. 1986. Revision of lithostratigraphic nomenclature in the Koobi Fora region, Kenya. *Journal of the. Geological Society, London*, **143**, 297–310.

Brown, F.H. and Nash, W.P. (1976). Radiometric dating and tuff mineralogy of Omo Group deposits. *In:* Coppens, Y., Howell, F.C., Isaac, G.L1. and Leakey, R.E.F. (eds) Earliest Man and Environments in the Lake Rudolf Basin., University of Chicago Press, 50-63.

Brown, F.H., McDougall, I., Davies, T. and Maier R. 1985. An integrated Plio-Pleistocene chronology for the Turkana basin. *In:* Delson, E. (ed.) Ancestors: The Hard Evidence, Alan R. Liss, New York, 82-90.

Brown, F.H., Haileab, B. and McDougall, I. 2006. Sequence of tuffs between the KBS Tuff and the Chari Tuff in the Turkana Basin, Kenya and Ethiopia. *Journal of the. Geological Society, London***, 163**, 185–204.

Campisano, C.J., Cohen, A.S., Arrowsmith, J.R., Asrat, A., Behrensmeyer, A.K., Brown, E.T., Deino, A.L., Deocampo, D.M., Feibel, C.S., Kingston, J.D., Lamb, H.F., Lowenstein, T.K., Noren, A., Olago, D.O., Owen, R.B., Pelletier, J.D., Potts, R., Reed, K.E., Renaut, R.W., Russell, J.M., Russell, J.R., Schäbitz, F., Stone, J.R., Trauth, M.H. and Wynn, J.G. 2017. The hominin sites and paleolakes drilling project: acquiring high-resolution paleoclimate records from the east African Rift system and their implications for understanding the environmental context of hominin evolution. PaleoAnthropology, 2017, 1 – 43.

Cashman, K., Sparks, R. and Blundy, J. 2017. Vertically extensive and unstable magmatic systems: A unified view of igneous processes. *Science,* **355**(6331), eaag3055.

Cerling, T.E. and Brown, F.H. 1982. Tuffaceous marker horizons in the Koobi Fora region and the Lower Omo Valley. *Nature*, **299**, 216–221.

Cerling, T.E., Brown, F.H., Cerling, B.W., Curtis, G.H. and Drake, R.E. 1979. Preliminary correlations between the Koobi Fora and Shungura Formations, East Africa. *Nature*, **279**, 118–121.

Channell, J.E.T., Singer, B.S. and Jicha, B.R. 2020. Timing of Quaternary geomagmetic reversals and excursions in volcanic and sedimentary archives. *Quaternary Science Rev*iews, **228**, 106114.

Chen, Y., Smith, P.E., Evensen, N.M., York, D. and Lajoie, K.R. 1996. The edge of time: Dating young volcanic ash layers with the ^{40}Ar-^{39}Ar laser probe. Science, 274 (5290), 1176-1178.

Cooper, K. and Kent, A. (2014). Rapid remobilization of magmatic crystals kept in cold storage. *Nature*, **506**(7489), 480–483.

Curtis, G. H., Drake, R. E., Cerling, T.E., Cering, B. W. and Hampel, J. H. 1975. Age of KBS Tuff in Koobi Fora Formation, East Rudolf, Kenya. *Nature*, **258**, 395-398.

Dart, R. 1925. *Australopithecus africanus* The Man-Ape of South Africa. *Nature*, **115**, 195–199.

de Heinzelin, J. (ed.) 1983. The Omo Group. Koninklijk Museum voor Midden-Afrika, Tervuren, Geologische Wetenschappen, 85.

Deino, A.L., Dommain, R., Keller, C.B., Potts, R., Behrensmeyer, A.K., Beverly, E.J., King, J., Heil, C.W., Stockhecke, M., Brown, E.T., Moerman, J., deMenocal, P. and the Olorgesailie Drilling Project Scientific Team 2019. Chronostratigraphic model of a high-resolution drill core record of the past million years from the Koora Basin, south Kenya Rift: Overcoming the difficulties of variable sedimentation rate and hiatuses. *Quaternary Science Reviews*, **215**, 213-231.

deMenocal, P.B. 1995. Plio-Pleistocene African climate. *Science*, **270**, 53-59.

Drake, R., Curtis, G. H., Cerling, T. E., Cerling, B. W. and Hampel, J. 1980. KBS Tuff dating and geochronology of tuffaceous sediments in the Koobi Fora and Shungura Formations, Eastern Africa. *Nature*, **283**, 368-372.

Feibel, C. S. 1983. Stratigraphy and paleoenvironments of the Koobi Fora Formation along the western Koobi Fora Ridge, East Turkana, Kenya. MS thesis, Iowa State University, Ames, Iowa.

Feibel, C.S., Brown, F.H. and McDougall, I. 1989. Stratigraphic context of fossil hominids from the Omo Group deposits: northern Turkana Basin, Kenya and Ethiopia. *American Journal of Physical Anthopology*, **78**, 595-622.

Feibel, C.S., Lepre, C.J. and Quinn, R.L. 2009. Stratigraphy, correlation, and age estimates for fossils from Area 123, Koobi Fora. *Journal of Human Evolution*, **57**, 112-122.

Fitch, F.J. and Miller, J.A. 1970. Radioisotope age determinations of Lake Rudolf artefact site: *Nature*, **226**, 226-228.

Fitch, F.J. and Miller, J.A. 1976. "Conventional potassium-argon and argon-40/argon-39 dating of volcanic rocks from East Rudolf". *In:* Coppens, Y., Howell, F. C., Isaac, G. LI., and Leakey, R.E.F. (eds) Earliest man and environments in the Lake Rudolf Basin, University of Chicago, Chicago, pp. 123-147.

Fitch, F.J., Miller, J.A. and Mitchell J.G. 1996. Dating of the KBS tuff and *Homo rudolfensis*. Journal of Human Evolution, **30**, 277-286.

Gathago, P.N. and Brown, F.H. 2006. Stratigraphy of the Koobi Fora Formation (Pliocene and Pleistocene) in the Ileret region of northern Kenya. *Journal of African Earth Sciences*, **45**, 369-390.

Harris, J.M., Brown, F.H. and Leakey, M.G. 1988. Stratigraphy and paleontology of Pliocene and Pleistocene localities west of Lake Turkana, Kenya. Natural History Museum of Los Angeles County, *Contributions in Science*, **399**, 1–128.

Gathago, P.N. and Brown, F.H. 2006. Stratigraphy of the Koobi Fora Formation (Pliocene and Pleistocene) in the Ileret region of northern Kenya. *Journal of African Earth Sciences*, **45**, 369-390.

Gleadow, A.J.W. 1980. Fission track age of the KBS Tuff and associated hominid remains in northern Kenya. *Nature*, **284**, 225-230.

Harris, J.M., Brown, F.H. and Leakey, M.G. 1988. Stratigraphy and paleontology of Pliocene and Pleistocene localities west of Lake Turkana, Kenya. Natural History Museum of Los Angeles County, *Contributions in Science*, **399**, 1–128.

Heizler, M.T., Karlstrom, K.E., Albonico, M., Hereford, R., Beard, L.S., Cather, S.M., Crossey, L.J. and Sundell, K.E. 2021. Detrital sanidine $^{40}Ar/^{39}Ar$ dating confirms <2 Ma age of Crooked Ridge paleoriver and subsequent deep denudation of the southwestern Colorado Plateau. *Geosphere*, **17**, 438-454.

Herries, A.I.R., Martin, J.M., Leece, A.B., Adams, J.W., Boschian, G., Joannes-Boyau, R., Edwards, T.R., Mallett, T., Massey, J., Murszewski, A., Neubauer, S., Pickering, R., Strait, D.S., Armstrong, B.J., Baker, S., Caruana, M.V., Denham, T., Hellstrom, J., Moggi-Cecchi, J., Mokobane, S., Penzo-Kajewski, P., Rovinsky, D.S., Schwartz, G.T., Stammers, R.C., Wilson, C., Woodhead, J. and Menter, C. 2020. Contemporaneity of *Australopithecus*, *Paranthropus*, and early *Homo erectus* in South Africa, *Science*, **368**, 1-19.

Horng, C.S., Lee, M.Y., Pälike, H., Wei, K.-Y., Liang, W.T., Iizuka, Y. and Torii, M. 2002. Astronomically calibrated ages for geomagnetic reversals within the Matuyama chron. Earth Planets Space, **54**, 679-690.

Hübert, J., Whaler, K. and Fisseha, S. 2018. The electrical structure of the Central Main Ethiopian Rift as imaged by Magnetotellurics — Implications for magma storage and pathways. *Journal of Geophysical Research: Solid Earth*, **123**, 6019–6032.

Hurford, A.J., Gleadow, A.J.W. and Naeser, C.W. 1976. Fission-track dating of pumice from the KBS Tuff, East Rudolf, Kenya. *Nature*, **263**, 738-740.

Iddon, F., Jackson, C., Hutchison, W., Fontijn, K., Pyle, D. M., Mather, T. A., Yirgu, G., and Edmonds, M. 2019. Mixing and crystal scavenging in the Main Ethiopian Rift revealed by trace element systematics in feldspars and glasses. *Geochemistry, Geophysics, Geosystems*, **20**(1), 230–259.

Joordens, J.C.A., Vonhof, H.B., Feibel, C.S., Lourens, L.J., Dupont-Nivet, G., van der Lubbe, H.J.L., Sier, M.J., Davies, G.R. and Kroon, D. 2011. An astronomically-tuned climate framework for hominins in the Turkana Basin. *Earth and Planetary Science Letters*, **307**, 1-8.

Joordens, C.A., Dupont-Nivet, G., Feibel, C.S., Spoor, F., Sier, M.J., van der Lubbe, J.H.J.L., Kellberg Nielsen, T., Knul, M.V., Davies, G.R. and Vonhof, H.B. 2013. Improved age control on early Homo fossils from the upper Burgi Member at Koobi Fora, Kenya. Journal of Human Evolution, **65**, 731-745.

Katoh, S., Nagaoka, S., WoldeGabriel, G., Renne, P., Snow, M.G., Beyene, Y. and Suwa, G. 2000. Chronostratigraphy and correlation of the Plio- Pleistocene tephra layers of the Konso Formation, southern Main Ethiopian Rift, Ethiopia. *Quaternary Science Reviews*, **19**, 1305–1317.

Keller C.B., Schoene, B. and Samperton, K.M. 2018. A stochastic sampling approach to zircon eruption age interpretation. *Geochemical Perspectives Letters*, **8**, 31-35.

Laskar, J., Robutel, P., Joutel, F., Gastineau, M., Correia, A.C.M. and Levrard, B. 2004. A long-term numerical solution for the insolation quantities of the Earth. *Astronomy and Astrophysics*, **428**, 261-285.

Leakey, M.D. 1970. Early artefacts from the Koobi Fora Area. *Nature*, **226**, 228-230.

Leakey, M.G., Spoor, F., Dean, M.G., Feibel, C.S., Anton, S.C., Kiarie, C. and Leakey, L.N. 2012. New fossils from Koobi Fora in northern Kenya confirm taxonomic diversity in early *Homo*. *Nature*, **488**, 201-204.

Leakey, R.E.F. 1974. Further evidence of Lower Pleistocene hominids from East Rudolf, North Kenya, 1973. *Nature*, **248,** 653-656.

Leaky, R.E.F. 1973. Evidence for an advanced Plio-Pleistocene hominid from East Rudolf, Kenya. *Nature*, **242**, 447-450.

Lee J.-Y., Marti K., Severinghaus J. P., Kawamura K., Yoo H.-S., Lee J. B. and Kim J. S. A. 2006. A. redetermination of the isotopic abundances of atmospheric Ar. *Geochimica et Cosmochimica Acta*, **70**, 6.

Lepre, C.J. and Kent, D.V. 2010. New magnetostratigraphy for the Olduvai Subchron in the Koobi For a Formation, northwest Kenya, with implications for early *Homo*. *Earth and Planetary Science Letters*, **290**, 362-374.

Lepre, C.J. and Kent, D.V. 2015. Chronostratigraphy of KNM-ER 3733 and other Area 104 hominins from Koobi Fora. Journal of Human Evolution, 86, 99-111.

Lepre, C.J., Quinn, R.L., Joordens, J.C.A., Swisher, C.C., III and Feibel, C.S. 2007. Plio-Pleistocene facies environments from the KBS Member, Koobi Fora Formation: implications for climate controls on the development of lake-margin hominin habitats in the northeast Turkana Basin (northwest Kenya). *Journal of Human Evolution*, **53**, 504–514.

Levin, N.E. 2015. Environment and Climate of Early Human Evolution. *Annual Review of Earth and Planetary Sciences*, **43**, 405-429.

Lewin, R. 1987. Bones of Contention, University of Chicago Press, 366p.

Lisiecki, L.E. and Ramo, M.E. 2005. A Pliocene-Pleistocene stack of 57 globally distributed benthic $d^{18}O$ records. *Paleooceanography.* **20**, PA1003.

Lo Bello, Ph., Feraud, G., Hall, C.M., York, D., Lavina, P. and Bernat, M. 1987. $^{40}Ar/^{39}Ar$ step-heating and laser fusion dating of a Quaternary pumice from Neschers, Massif Central, France: the defeat of xenocrystic contamination. Chemical Geology (Isotope Geoscience) 66, 61-71.

Lourens, L. Hilgen, F. Shackleton, N. Laskar, J. Wilson, D. 2004. "The Neogene Period". *In:* Gradstein, *F.,* Ogg, J. and Smith, J., A. (eds) A Geologic Time Scale, Cambridge University Press, pp. 409 – 440.

Lourens, L.J., Antonarakou, A., Hilgen, F.J., Van Hoof, A.A.M., Vergnaud-Grazzini and C., Zachariasse, W.J. 1996. Evaluation of the Plio-Pleistocene astronomical timescale. *Paleoceanography*, **11**, 391e413.

Ludwig, K.R. 2012. User's Manual for Isoplot 3.75. A Geochronological Toolkit for Microsoft Excel: *Special Publication. No. 5, Berkeley Geochronology Center, Berkeley, California*, 75p.

Lupien, R.L., Russell, J.M., Grove, M., Beck, C.C., Feibel, C.S. and Cohen, A.S. 2020. Abrupt climate change and its influences on hominin evolution during the early Pleistocene in the Turkana Basin, Kenya. *Quaternary Science Reviews*, **245**, 106531.

Lupien, R., Russell, J., Feibel, C., Beck, C., Casta~neda, I., Deino, A. and Cohen, A. 2018. A leaf wax biomarker record of early Pleistocene hydroclimate from West Turkana, Kenya. *Quaternary Science Reviews*, **186**, 225e235.

McDougall, I. 1981. $^{40}Ar/^{39}Ar$ age spectra from the KBS Tuff, Koobi Fora Formation. *Nature*, **294**, 120-124.

McDougall, I. Maier, R. Sutherland-Hawkes, P. A.J.W. Gleadow, K-Ar estimate for the KBS Tuff, East Turkana, Kenya. *Nature* **284**, 230-234. (1980).

McDougall, I. 1985. K-Ar and $^{40}Ar/^{39}Ar$ dating of the hominid-bearing Pliocene-Pleistocene sequence at Koobi Fora, Lake Turkana, northern Kenya. *Geological Society of America Bulletin*, **96(2)**, 159-175.

McDougall, I. and Brown, F.H. 2006. Precise $^{40}Ar/^{39}Ar$ geochronology for the upper Koobi Fora Formation, Turkana Basin, northern Kenya. *Journal of the Geological Society, London*, **163**, 205-220.

McDougall, I. and Brown, F.H. 2008. Geochronology of the pre-KBS Tuff sequence, Omo Group, Turkana Basin. *Journal of the. Geological Society, London,* **165**, 549-562.

McDougall, I., Brown, F.H., Vasconcelos, P.M., Cohen, B.E., Thiede, D.S. and Buchanan, M.J. 2012. New single crystal $^{40}Ar/^{39}Ar$ ages improve time scale for deposition of the Omo Group, Turkana Basin, Eastern Africa. *Journal of the Geological Society, London*, **169**, 213-226.

Min, K.W., Mundil, R., Renne, P.R. and Ludwig, K.R. 2000. A test for systematic errors in $^{40}Ar/^{39}Ar$ geochronology through comparison with U/Pb analysis of a 1.1-Ga rhyolite. *Geochimica et Cosmochimica Acta* **64**, 73-98.

Nutz, A., Schuster, M., Boës, X. and Rubino, J-L. 2017. Orbitally-driven evolution of Lake Turkana (Turkana Depression, Kenya, EARS) between 1.95 and 1.72 Ma: A sequence stratigraphy perspective. *Journal of African Earth Sciences*, **125**, 230-243.

Phillips D. and Matchan, E.L. 2013. Ultra-high precision $^{40}Ar/^{39}Ar$ ages for Fish Canyon Tuff and Alder Creek Rhyolite sanidine: new dating standards required? *Geochimica et Cosmochimica Acta,* **121**, 229-239.

Phillips, D., Matchan, E.L., Dalton, H. and Kuiper, K.F. 2022. Revised astronomically calibrated $^{40}Ar/^{39}Ar$ ages for the Fish Canyon Tuff sanidine – closing the interlaboratory gap. *Chemical Geology*, **597,** 120815.

Potts, R. 2013. Hominin evolution in settings of strong environmental variability. *Quaternary Science Rev*iews, **73**, 1-13.

Powell, R., Green, E.C.R., Marillo Sialer, E. and Woodhead, J. 2020. Robust isochron calculation. *Geochronology*, **2**, 325-342.

Raynolds, R. 2017. *Geologic map of the Karari Ridge*. turkanastratigraphy.org.

Renne, P.R., Sharp, Z,D. and Heizler, M.T. 2008. Cl-derived argon isotope production in the CLICIT facility of OSTR reactor and the effects of the Cl-correction in $^{40}Ar/^{39}Ar$ geochronology. *Chemical Geology*, **255**, 463-466.

Sano, K., Beyene, Y., Katoh, S., Koyabu, D., Endo, H. , Sasaki, T. , Asfaw, B., and Gen Suwa, G. 2020. 1.4-million-year-old bone handaxe from Konso, Ethiopia, shows advanced tool technology in the early Acheulean. *Proceedings of the National Academy of Sciences,* **117 (31)**, 18393-18400.

Schaen, A.J., Jicha, B.R., Hodges, K.V., Vermeesch, P., Stelten, M.E., Mercer, C.M., Phillips, D., Rivera, T.A., Jourdan, F., Matchan, E.L., Hemming, S.R., Morgan, L.E., Kelley, S.P., Cassata, W.S., Heizler, M.T., Vasconcelos, P.M., Benowitz, J.A., Koppers, A.A.P., Mark, D.F., Niespolo, E.M., Sprain, C.J., Hames, W.E., Kuiper, K.F., Turrin, B.D., Renne, P.R., Ross, J., Nomade, S., Guillou, H., Webb, L.E., Cohen, B.A., Calvert, A.T., Joyce, N., Ganerød, M., Wijbrans, J., Ishizuka, O., He, H., Ramirez, A., Pfänder, J.A., Lopez-Martínez, M., Qiu, H. and Singer, B.S. 2021. Interpreting and reporting $^{40}Ar/^{39}Ar$ geochronologic data. *Geological Society of America Bulletin,* **133** (3-4): 461–487.

Shackleton, N.J., Berger, A. and Peltier, W.R. 1990. An alternative astronomical calibration of the lower Pleistocene timescale based on ODP Site 677. *Transactions of the Royal Society of Edinburgh. Earth Science,* **81**, 251e261.

Sparks, R. S. J., Annen, C., Blundy, J.D., Cashman, K.V., Rust, A.C. and Jackson, M.D. 2019. Formation and dynamics of magma reservoirs. *Philosophical Transactions of the Royal Society A Mathematical, Physical and Engineering Sciences*, **377**, 20180019 (2019).

Stelten, M.E., Cooper, K.M., Vazquez, J.A., Calvert, A.T. and Glessner, J.J.G. 2015. Mechanisms and Timescales of Generating Eruptible Rhyolitic Magmas at

Yellowstone Caldera from Zircon and Sanidine Geochronology and Geochemistry. *Journal of Petrology*, **56(8)**, 1607-1642.

Tiedemann, R., Sarnthein, M. and Shackleton, N.J. 1994. Astronomic timescale for the Pliocene Atlantic delta-O-18 and dust flux records of ocean drilling program site 659. *Palaeoceanography*, **9(4),** 619–638.

Tindall, K.W. 1985. *Stratigraphy and sedimentology of the Koobi Fora Formation, eastern Koobi Fora Ridge, east Turkana, Kenya*. MS thesis, Iowa State University, Ames.

Van den Bogaard, P., Hall, C.M., Schmincke, H.-U. and York, D. 1989. Precise laser $^{40}Ar/^{39}Ar$ dating of a cold to warm climate transition in Central Europe. Nature, 342, 523-525.

van der Lubbe, H.J.L., Krause-Nehring, J., Junginger, A., Garcin, Y., Joordens, J.C.A., Davies, G.R., Beck, C., Feibel, C.S., Johnson, T.C. and Vonhof, H.B. 2017. Gradual or abrupt?Changes in water source of Lake Turkana (Kenya) during the African Humid Period inferred from Sr isotope ratios. *Quaternary Science Reviews*, **174**, 1-12.

van der Lubbe, H.J.L., Hall, I.R., Barker, S., Hemming, S.R., Baars, T.F., Starr, A., Just, J., Backeberg, B.C. and Joordens, J.C.A. 2021. Indo-Pacific Walker circulation drove Pleistocene African aridification. *Nature*, **598**, 618-623.

Van Zalinge, M.E., Mark, D.F., Sparks, R.S.J., Tremblay, M.M., Keller, C.B., Cooper, F.J. and Rust, A. 2022. Timescales for pluton growth, magma-chamber formation and super-eruptions. Nature, **608**, 87-92.

Woldegabriel, G., Hart, W.K., Katoh, S., Beyene, Y. and Suwa, G. (2005). Correlation of Plio-Pleistocene Tephra in Ethiopian and Kenyan rift basins: Temporal calibration of geological features and hominid fossil records. *Journal of Volcanology and Geothermal Research*, **147** (1–2), 81–108.

Wood, B. and Leakey, M. 2011. The Omo-Turkana Basin Fossil Hominins and Their Contribution to Our Understanding of Human Evolution in Africa. *Evolutionary Athropology*, **20**, 264-292.

Yancey, T.E., Heizler, M.T., Miller, B.V. and Guillemette, R.N. 2018. Eocene–Oligocene chronostratigraphy of ignimbrite flareup volcanic ash beds on the Gulf of Mexico coastal plains. *Geosphere*, **14**, 1232–1252.

Figures Captions

Fig. 1 (**a**) Regional geological map of the Turkana Basin (modified after McDougall and Brown 2006), showing the contemporaneous Koobi Fora, Nachukui and Shungura Formations. Sample localities shown as red filled circles. (**b**) Simplified stratigraphic section of the Koobi Fora and Shungura Formations (modified after McDougall and Brown 2006). Ages in red text are from this study.

Fig. 2 Previous age data for (**a**) KBS/H2 and Malbe/H4 tuffs and (**b**) Chari/Tuff L and Gele tuffs. Ages recalculated using decay constants of Min et al. (2000) and fluence monitor ages of Phillips et al. (2022). F&M'70 = Fitch and Miller (1970); F&M'76 = Fitch and Miller (1976) B&N = Brown and Nash (1976); McD'80 = McDougall et al. (1980); McD'85 = McDougall (1981); McD'85 = McDougall (1985); McD&B'06 = McDougall and Brown (2006). Error bars shown with 2σ uncertainties.

Fig. 3 Representative major element variation diagrams for tuff and pumice glass shards from current KBS (=H2), Malbe (=H4), Chari (=L) and Gele tuff samples. Tuff glass samples are ETH86-279 (KBS), K80-225 (Malbe), K03-0069 (Chari) and K82-835 (Gele). The remaining sample numbers refer to pumice glass fragments. EMPA source data are listed in Table S3.

Fig. 4 Ternary feldspar diagrams with field lines after Deer et al. (1992). Source EMPA data are listed in Table S4. (**a**) KBS/H2 Tuff pumice feldspar compositions, (**b**) Malbe/H4 Tuff pumice feldspar compositions, (**c**) Chari/Tuff L pumice feldspar compositions and (**d**) Gele Tuff pumice feldspar compositions.

Fig. 5 $^{40}Ar/^{39}Ar$ single-fragment feldspar ages (in ka) for (**a**) KBS/H2 samples, (**b**) Malbe/H4 samples, (**c**) Chari/Tuff L samples and (**d**) Gele samples. Preferred eruption age estimates (Table 1) were calculated using the Bayesian algorithm of Keller et al. (2018). Vertical bars indicate 2σ uncertainties. Source data are listed in Table S5.

Fig. 6 Composite $^{40}Ar/^{39}Ar$ ages (ka) for (**a**) KBS/H2 feldspars, (**b**) Malbe/H4 feldspars, (**c**) Chari/Tuff L feldspars and (**d**) Gele feldspars. Listed eruption age estimates are

calculated using the Bayesian algorithm of Keller et al. (2018). Vertical bars indicate 2σ uncertainties. Source data are listed in Table S5.

Fig. 7 $^{40}Ar/^{39}Ar$ ages versus Ca/K ratios for (**a**) KBS/H2 feldspars, (**b**) Malbe/H4 feldspars, (**c**) Chari/Tuff L feldspars and (**d**) Gele feldspars. Note the broad correlation in ages with Ca/K ratios for the Chari/Tuff L and Gele feldspars. Vertical and horizontal bars indicate 2σ uncertainties. Source data are listed in Table S5.

Fig. 8 Composite $^{40}Ar/^{39}Ar$ dataset from Chari/Tuff L samples showing eruption age estimates calculated using several statistical approaches. The nMAD plus 'gap' algorithm method (e.g. Deino et al. 2019) typically gives the oldest estimates, followed by Model 3 (Normality test and goodness-of-fit filter; Andersen et al. 2017). Models 1 (low MSWD weighted mean) and 2 (weighted mean filter) (Schaen et al. 2020) and the Bayesian algorithm (Keller et al. (2018) give similar younger ages, with the more conservative Bayesian age estimates preferred.

Fig. 9 Probability density plot showing recalculated $^{40}Ar/^{39}Ar$ data from the four Chari Tuff samples analysed by McDougall and Brown (2006). The calculated weighted mean age for the four samples (1384.5 ± 7.9 ka) is distinctly older than the Bayesian age estimate (1359.2 ± 7.5 ka) (n = 46 of 56 feldspars), with the latter indistinguishable from current results.

Fig. 10 Orbital tuning of fossiliferous sediments below the KBS Tuff: **(*a*)** Simplified stratigraphic sequence for the Upper Burgi Member (Koobi Fora Formation) below the KBS Tuff (adapted from Joordens et al. 2011). Fish fossils extracted from these sediments were analysed for Sr isotopic compositions (Joordens et al. 2011, 2013). **(*b*)** 65°N summer insolation curve of the $La2004_{(1,1)}$ solution (Laskar et al. 2004) for the time interval 1860 – 2000 ka (maximum isolation i-cycles labelled). Wetter climatic periods are associated with insolation maxima (blue bars); drier periods with insolation minima. Also shown are the positions of Mediterranean deep-sea sapropel units (47 – 53; Lourens et al. 1996). **(*c*)** North African dust records from Mediterranean and Atlantic Ocean marine records (Tiedemann et al. 1994). Elevated levels of aeolian terrestrial dust accumulations are associated with reduced Mediterranean monsoonal

activity and drier climatic periods. ***(d)*** Revised tuning model (Model I) for the UBM in Areas 102 and 105, based on $^{87}Sr/^{86}Sr$ isotopic data from fish fossils (Joordens et al. 2011), and calibrated to the new KBS age of 1879.1 ± 2.4 ka (Table S7). This tuning model indicates an age 1975 ± 2 ka for the base of the Olduvai Subchron (bC2n), which is older than the previously reported values of 1945 ka (Horng et al. 2002) and 1925 ka (Channell et al. 2020), and links bC2n to an insolation minimum rather than the maximum inferred from ODP data (Lourens et al. 2004; Lisiecki and Ramo 2005). **(e)** $^{87}Sr/^{86}Sr$ isotopic data for UBM fish fossils in sediments below the KBS Tuff in Area 131 (Joordens et al. 2013) relative to the GPTS bC2n age. ***(f)*** Alternative tuning model (Model II) for the UBM in Areas 102 and 105 (Joordens et al. 2011) (Table S7). $^{87}Sr/^{86}Sr$ isotopic cycles above the sandy units are referenced to the age of the KBS tuff (1879.1 ± 2.4 ka), whereas cycles below the sandy units are referenced to a bC2n age of 1968 ka (Lisiecki and Ramo 2005). This tuning model requires a change in local or regional hydrodynamic patterns in the middle of the UBM (e.g. van der Lubbe et al. 2021).

Fig. 11 Estimates of hominin fossil ages from strata above and below the KBS Tuff in the Koobi Fora Formation. Coloured symbols represent age estimates from the current study. Grey bars indicate age estimates from previous studies (Feibel et al. 1989, 2009; Leakey et al. 2012; Joordens et al. 2013).

Tables

Table 1 Summary of $^{40}Ar/^{39}Ar$ age results for the KBS (=H2), Malbe (=H4), Chari (=L) and Gele tuffs, Turkana Basin.

Figure 1

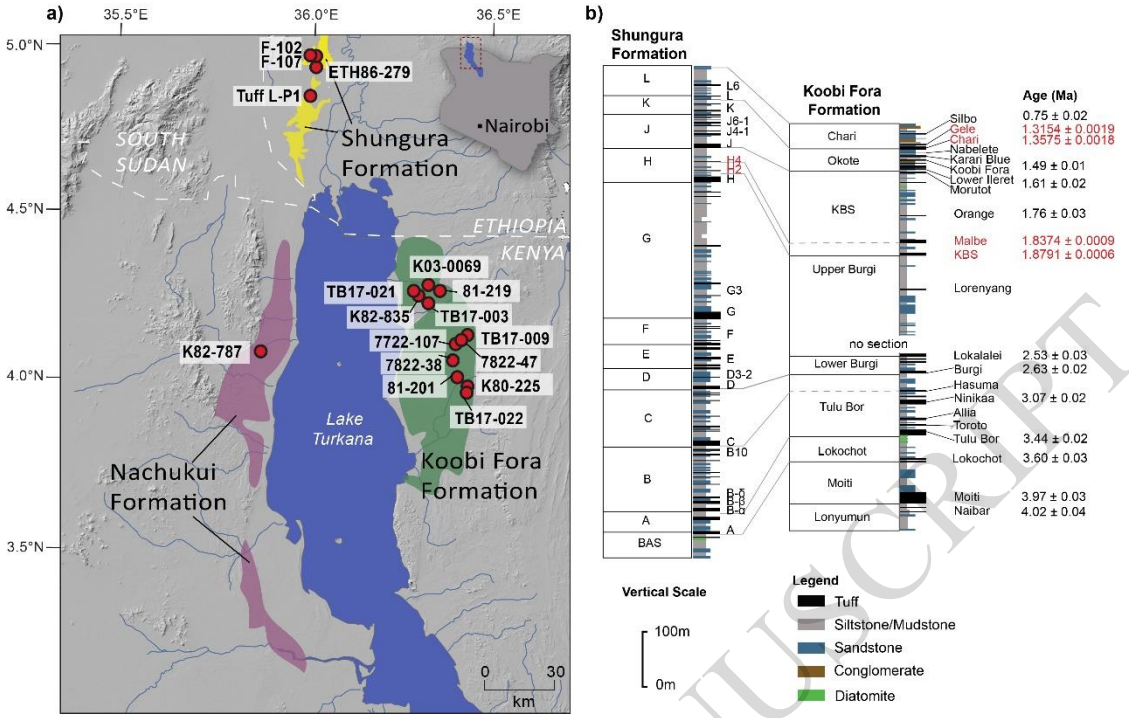

Figure 2

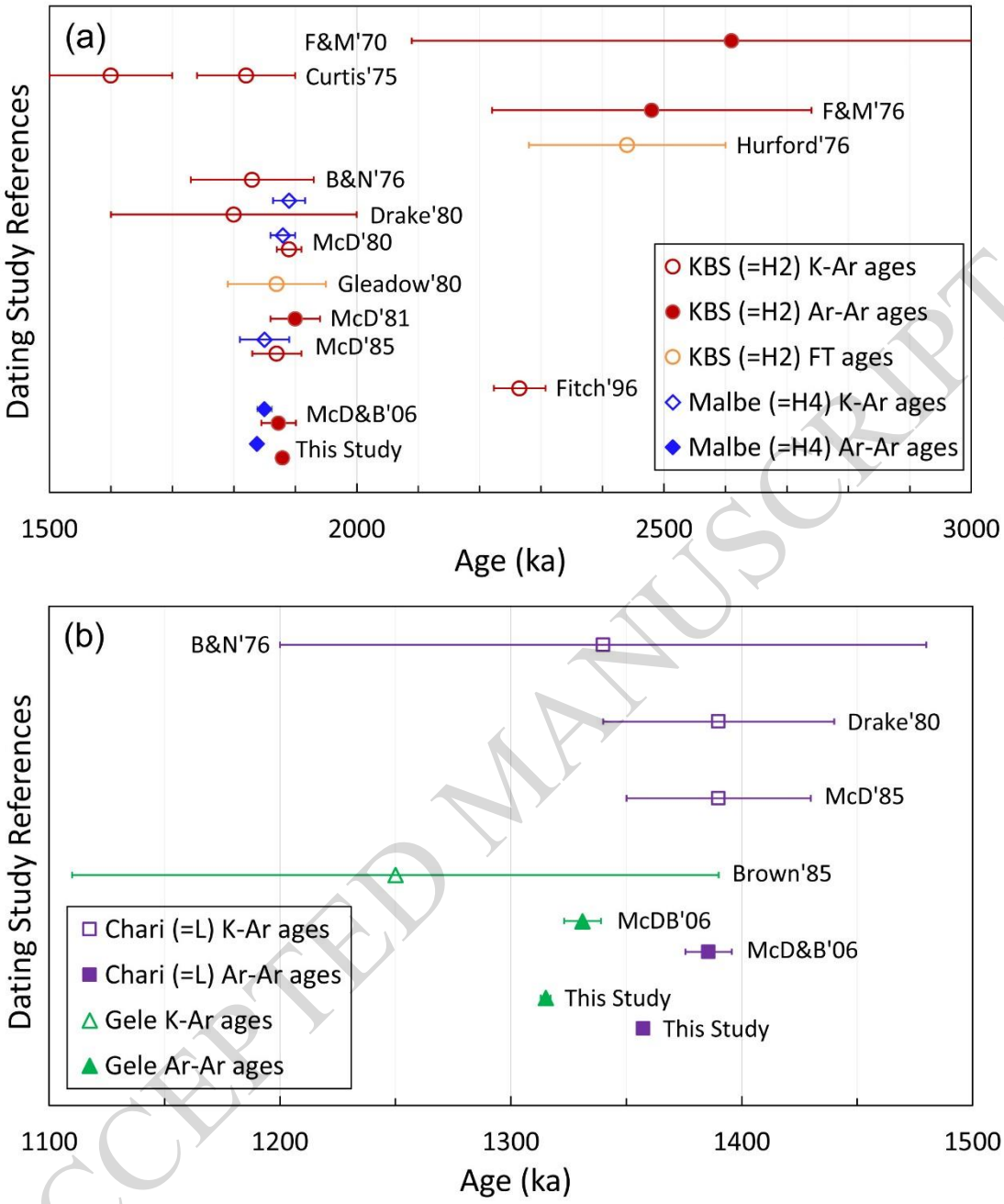

Figure 3

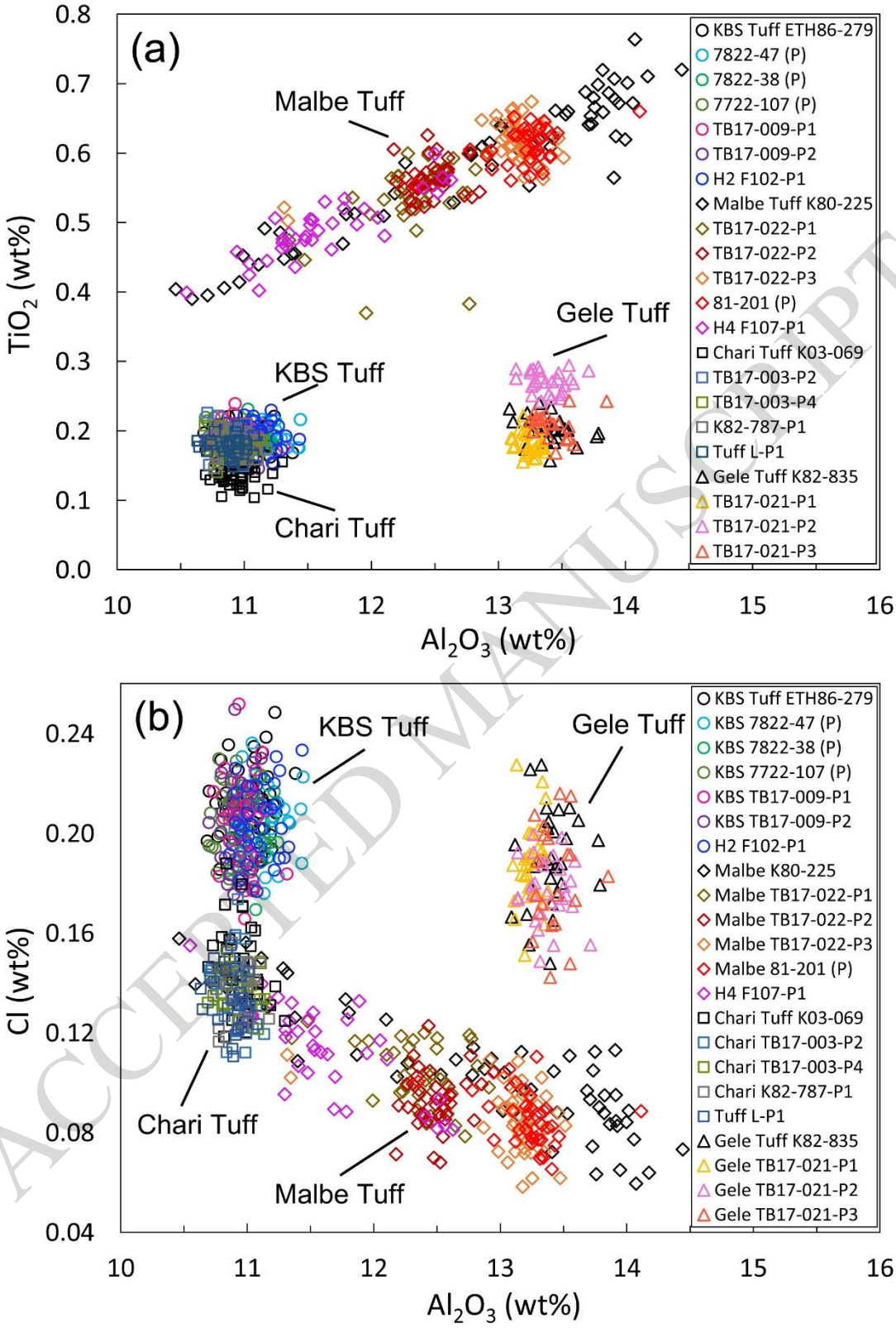

Figure 4

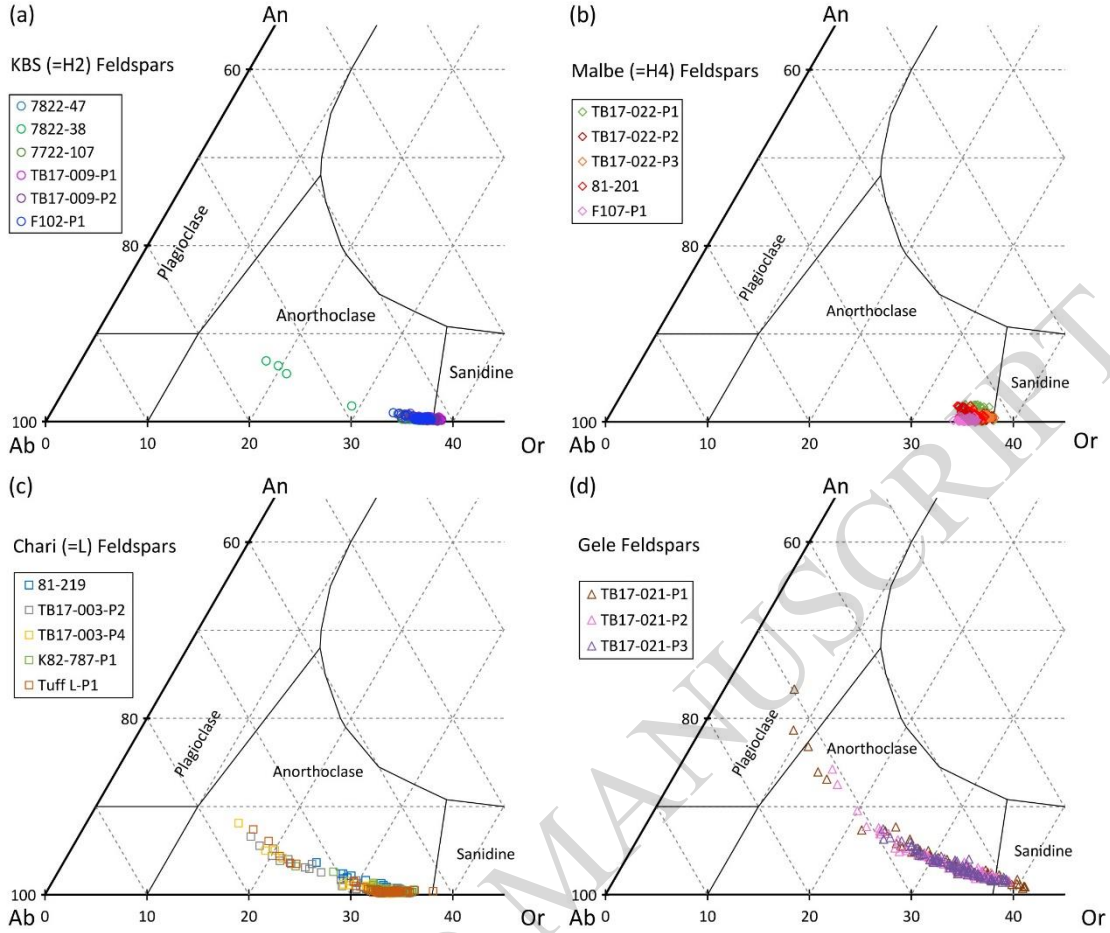

Figure 5

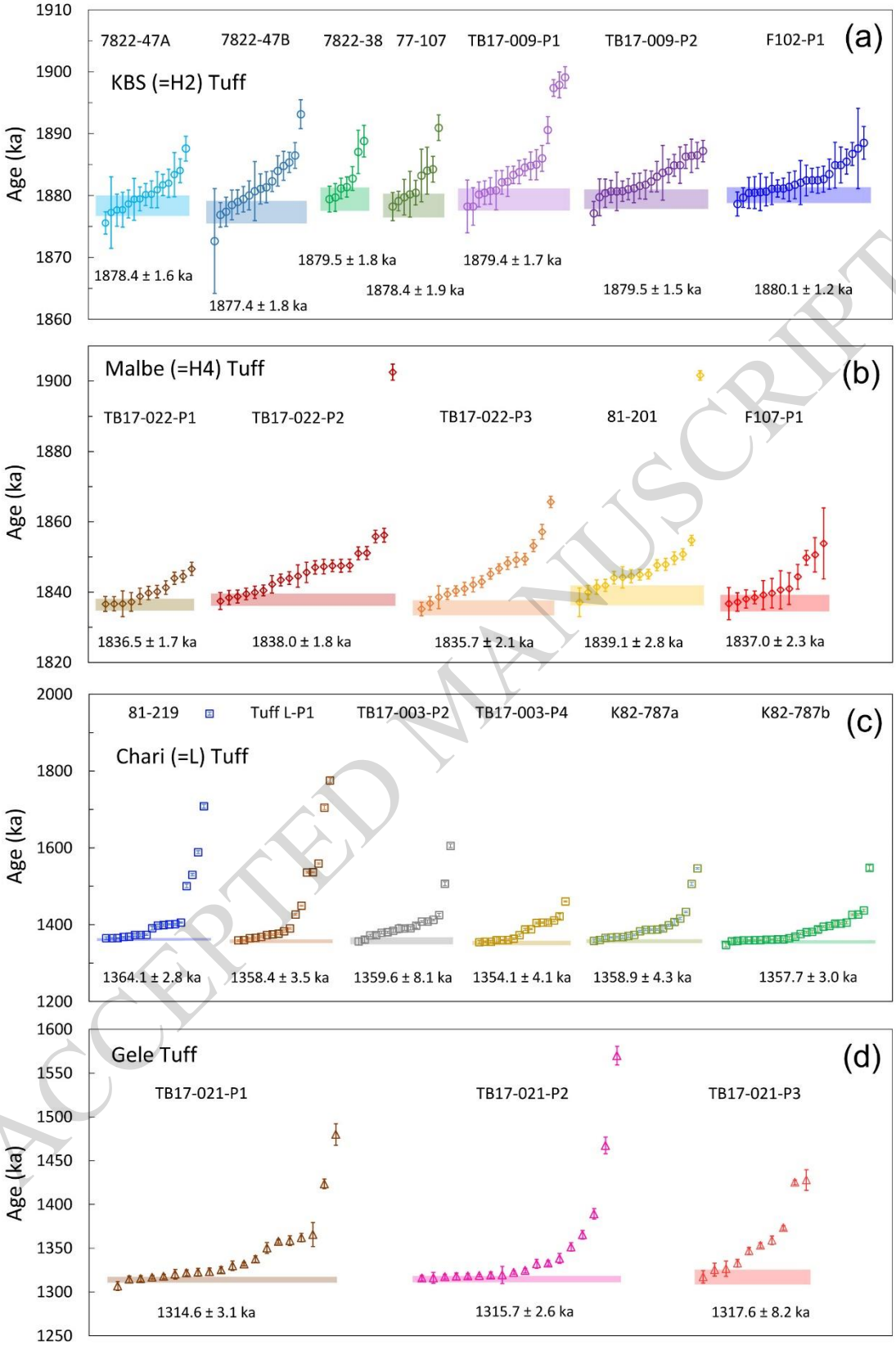

Figure 6

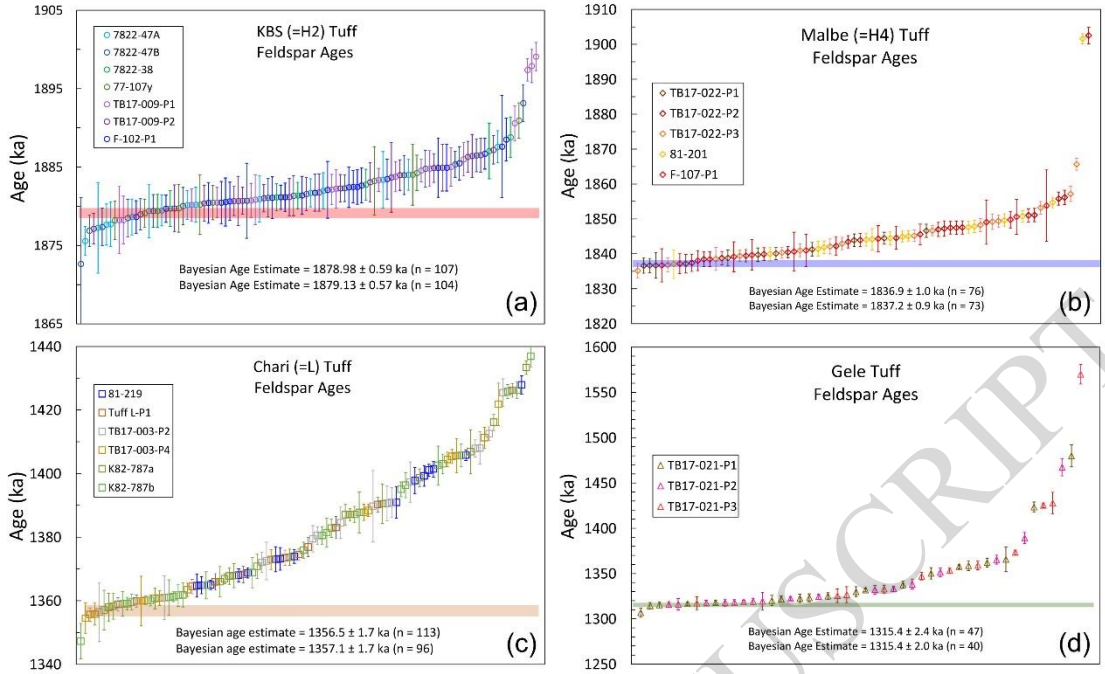

Figure 7

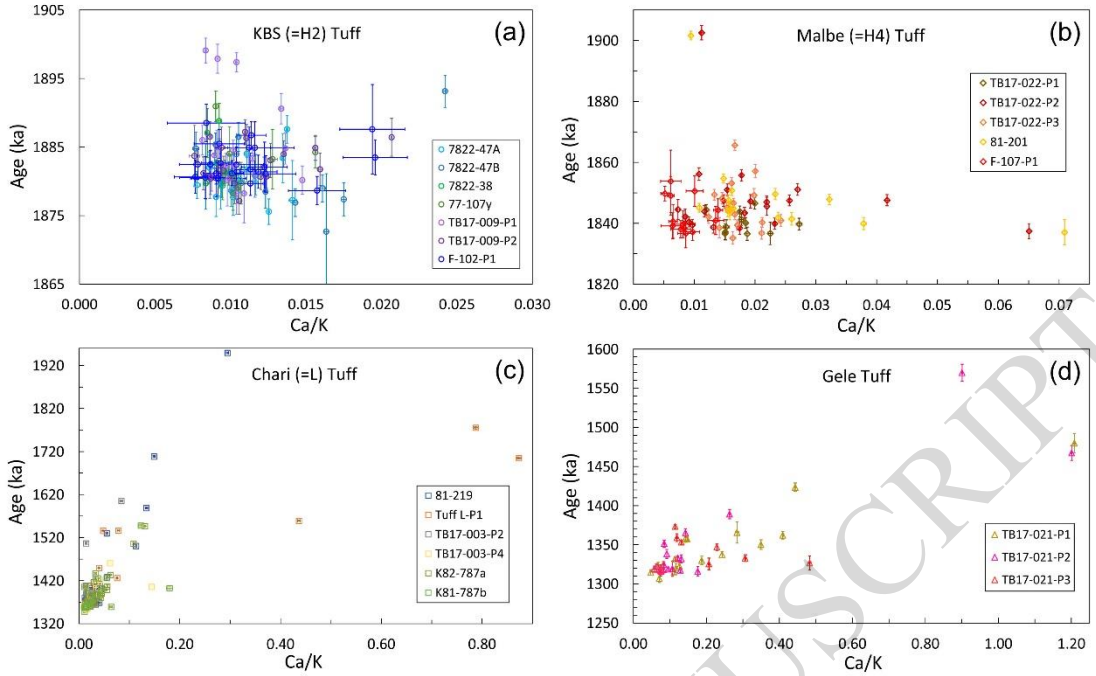

Figure 8

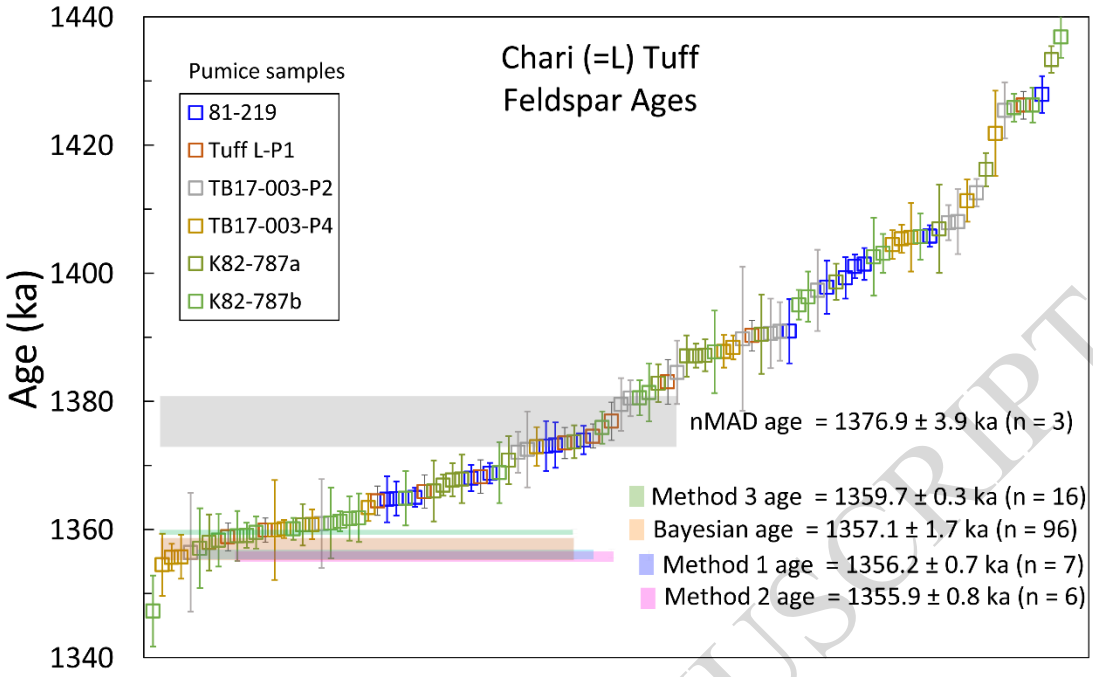

Figure 9

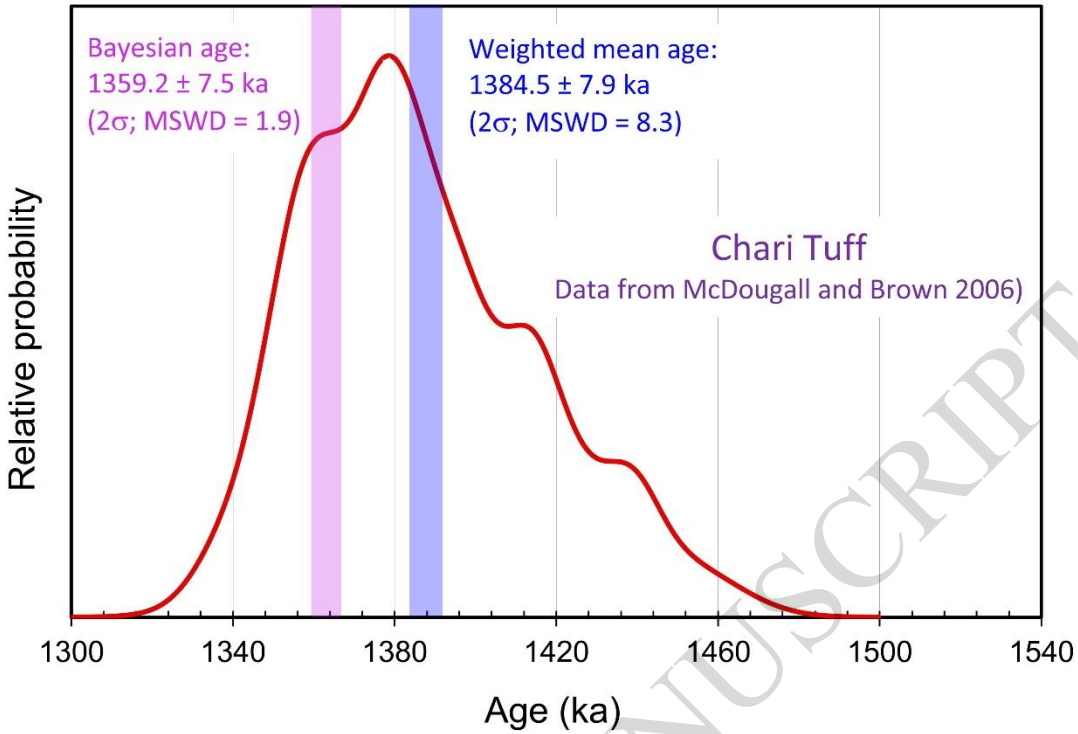

Figure 10

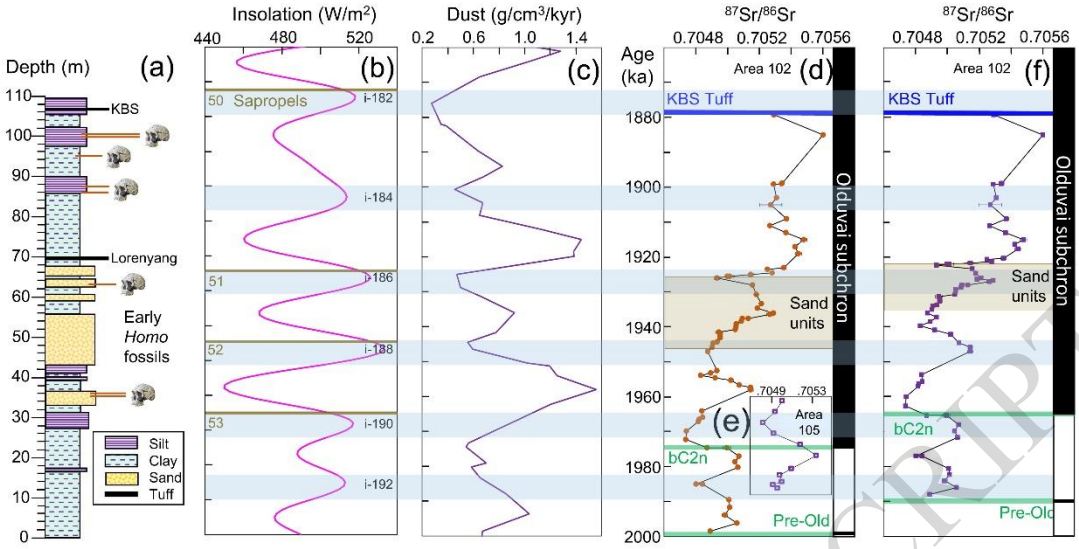

Figure 11

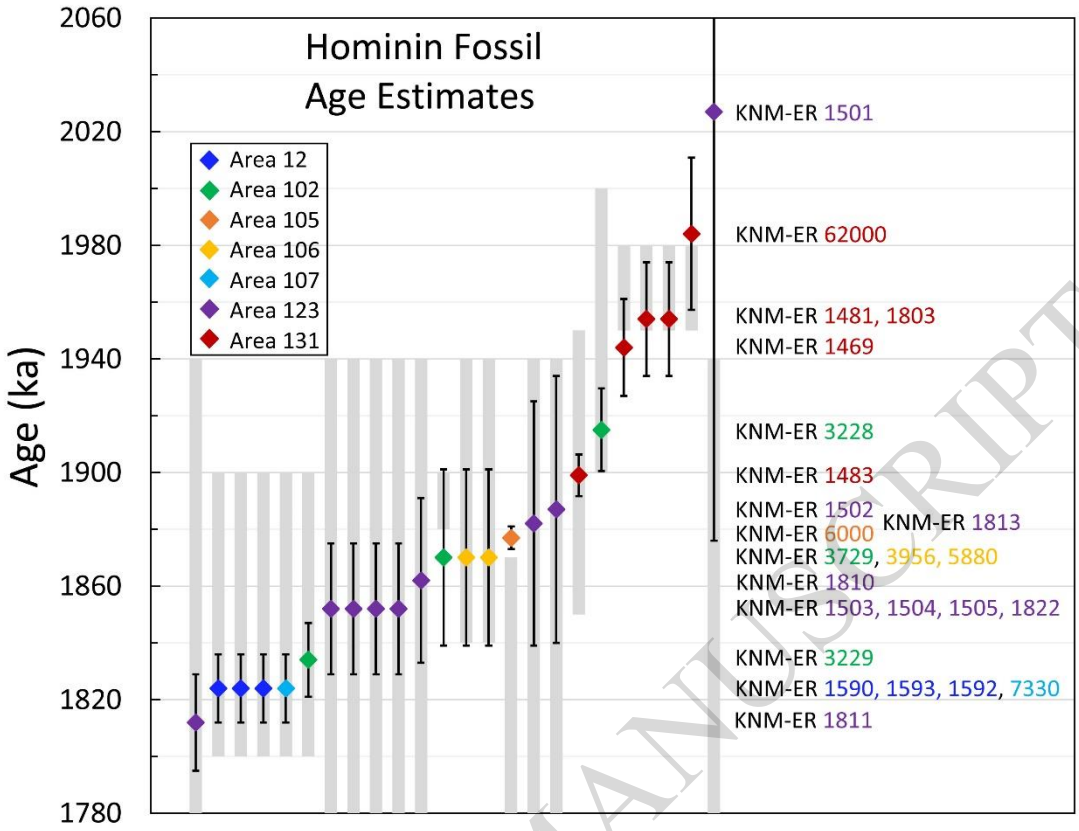

Table 1. Summary of $^{40}Ar/^{39}Ar$ age results for the KBS (=H2), Malbe (=H4), Chari (=L) and Gele tuffs, Turkana Basin.

Tuff	Sample #	N	nMAD Age Estimates (ka)				Method 1 Age Estimates (ka)					Method 2 Age Estimates (ka)					Method 3 Age Estimates (ka)					Bayesian Age Estimates (ka)					
			Age (ka)	± 2σ	MSWD	p	n	Age (ka)	± 2σ	MSWD	p	n	Age (ka)	± 2σ	MSWD	p	n	Age (ka)	± 2σ	MSWD	p	n	Age (ka)	± 2σ	Incl. ext. unc. (2σ)	MSWD	p	n
KBS (=H2)	7822-47A	15	1880.1	0.8	1.8	0.05	12	1877.3	1.1	1.4	2.40	7	1878.5	0.8	2.3	0.02	9	1880.1	0.8	1.8	0.05	12	1876.8	1.8				15
																							1878.4	1.6				14 [1]
	7822-47B	16	1880.3	1.4	3.0	0.00	10	1878.8	0.9	1.6	0.11	9	1878.8	0.9	1.6	0.11	9	1879.0	0.9	1.9	0.05	10	1877.4	1.8				16
																							1877.5	1.7				15 [1]
	7822-38	7	1881.0	0.9	1.8	0.12	5	1881.0	0.9	1.8	0.12	5	1880.6	1.0	1.1	0.35	4	1881.0	0.9	1.8	0.12	5	1879.5	1.8				7
	77-107y	9	1879.9	1.3	1.8	0.10	7	1879.9	1.3	1.8	0.10	7	1879.9	1.3	1.8	0.10	7	1879.9	1.3	1.8	0.10	7	1878.4	1.9				9
	TB17-009-P1	18	1883.5	1.2	3.0	0.00	11	1880.8	0.9	1.2	0.31	8	1880.6	1.0	1.1	0.36	7	1880.8	0.9	1.2	0.31	8	1879.4	1.7				18
	TB17-009-P2	20	1881.7	0.7	1.6	0.09	14	1877.1	2.0	n/a	n/a	1	1877.9	1.6	2.2	0.14	2	1881.5	0.7	1.3	0.22	13	1879.5	1.5				20
								1881.5	0.7	1.3	0.22	13 [1]	1881.2	0.8	0.7	0.75	11 [1]						1880.5	1.2				19 [1]
H2 (=KBS)	H2 F102-P1	23	1881.8	0.9	1.2	0.26	18	1881.3	0.9	1.5	0.08	18	1881.2	0.9	1.5	0.15	17	1881.3	0.9	1.5	0.08	18	1880.1	1.2				23
																							1880.4	1.2				22 [1]
Weighted Mean (samples)		*7*	*1881.2*	*1.9*	*5.1*	*0.00*	*7*	*1879.9*	*1.4*	*2.1*	*0.05*	*7*	*1879.7*	*0.8*	*1.5*	*0.19*	*7*	*1880.6*	*0.9*	*4.3*	*0.00*	*7*	*1878.9*	*1.1*	*2.6*	*2.3*	*0.03*	*7*
		7	*1881.0*	*0.9*	*3.2*	*0.01*	*6 [2]*	*1880.3*	*1.3*	*2.3*	*0.03*	*7 [1]*	*1880.1*	*0.7*	*1.7*	*0.12*	*7 [1]*	*1880.9*	*0.4*	*2.1*	*0.06*	*6 [3]*	*1879.1*	*0.6*	*2.4*	*1.3*	*0.23*	*7 [4]*
Weighted Mean (composite)		*108*	*1881.4*	*0.4*	*2.4*	*0.00*	*82*	*1879.1*	*0.4*	*1.3*	*0.08*	*36*	*1880.3*	*0.4*	*2.0*	*0.00*	*66*	*1880.7*	*0.3*	*1.3*	*0.05*	*64*	*1879.0*	*0.6*	*2.4*			*107 [4]*
																							1879.1	*0.6*	*2.4*			*104 [4,5]*
Malbe (=H4)	TB17-022-P1	11	1839.1	1.7	2.7	0.01	7	1837.8	1.0	1.6	0.16	6	1837.8	1.0	1.6	0.16	6	1837.8	1.0	1.6	0.16	6	1836.5	1.7				11
	TB17-022-P2	21	1845.8	1.5	4.0	0.00	10 [5]	1839.3	0.9	1.3	0.28	6	1839.0	1.0	0.9	0.47	5	1839.6	0.9	1.9	0.08	7	1838.0	1.8				21
																							1838.2	1.6				20 [5]
	TB17-022-P3	16	1842.8	2.7	5.4	0.00	5 [5]	1836.0	1.5	1.4	0.23	2	1836.0	1.5	1.4	0.23	2	1840.4	1.0	1.5	0.19	5	1835.7	2.1				16
																							1835.7	2.1				15 [5]
																							1837.4	2.1				14 [1,5]
	81-201	15	1844.7	0.9	0.3	0.90	5 [5]	1839.4	1.8	1.6	0.21	2	1840.3	1.4	2.0	0.14	3	1844.2	0.8	2.0	0.07	6	1839.1	2.8				15
																							1839.9	2.4				14 [5]
H4 (=Malbe)	F107-P1	12	1838.9	1.6	1.8	0.07	9	1838.9	1.6	1.8	0.07	9	1838.3	1.6	0.4	0.85	7	1838.9	1.6	1.8	0.07	9	1837.0	2.3				12
Weighted Mean (samples)		*5*	*1843.1*	*3.8*	*19*	*0.00*	*5 [5]*	*1838.4*	*1.6*	*4.4*	*0.00*	*5*	*1838.3*	*1.7*	*5.1*	*0.00*	*5*	*1840.7*	*3.4*	*29*	*0.00*	*5*	*1837.1*	*0.9*	*2.4*	*1.4*	*0.24*	*5*
			1838.8	*0.6*	*1.9*	*0.13*	*4 [6]*	*1838.7*	*1.6*	*2.9*	*0.03*	*4 [6]*	*1839.2*	*1.8*	*4.6*	*0.00*	*4 [7]*	*1837.4*	*0.9*	*2.4*	*2.3*	*0.06*	*5 [5]*
																							1837.7	*0.9*	*2.4*	*1.5*	*0.19*	*5 [5,8]*
Weighted Mean (composite)		*75*	*1843.9*	*0.7*	*2.6*	*0.00*	*27*	*1838.0*	*0.5*	*1.3*	*0.17*	*21*	*1838.8*	*0.6*	*2.0*	*0.00*	*28*	*1839.4*	*0.4*	*1.4*	*0.08*	*28*	*1836.9*	*1.0*	*2.5*			*76*
																							1837.2	*0.9*	*2.4*			*73 [5]*
Chari (=L)	81-219	19	1373.6	1.7	0.1	0.88	3 [5]	1364.9	1.3	0.02	0.98	3	1364.8	2.2	0.0	0.96	2	1365.7	1.1	2.5	0.06	4	1364.7	4.2				19
																							1364.1	2.8				14 [5]
L (=Chari)	L-P1	17	1370.7	32.8	8.8	0.00	2 [5]	1359.4	1.4	0.6	0.45	2	1358.8	2.1	n/a	n/a	1	1366.0	1.4	2.5	0.09	3	1358.5	6.3				17
																							1358.4	3.5				10 [5]
Chari (=L)	TB17-003-P2	17	1390.2	5.7	2.6	0.03	5 [5]	1359.4	5.6	0.6	0.44	2	1356.4	9.2	n/a	n/a	1	1381.3	2.1	1.7	0.17	4	1358.4	8.5				17
													1370.3	3.0	8.6	0.00	2						1359.6	8.1				15 [5]
	TB17-003-P4	16	1372.9	3.0	n/a	n/a	1 [5]	1355.7	1.7	0.5	0.70	4	1355.5	1.7	0.1	0.90	3	1355.7	1.7	0.5	0.70	4	1354.1	4.2				16
																							1354.1	4.1				15 [5]
	K82-787a	19	1385.5	8.2	3.4	0.03	3 [5]	1359.7	2.6	1.1	0.31	2	1359.7	2.6	1.1	0.31	2	1367.5	1.2	1.1	0.38	5	1358.5	5.0				19
																							1358.9	4.3				17 [5]
	K82-787b	26	1360.3	0.9	1.2	0.28	11 [5]	1347.3	5.5	n/a	n/a	1	1347.3	5.5	n/a	n/a	1	1360.3	0.9	1.2	0.28	11	1351.3	6.3				26
								1360.3	0.9	1.2	0.26	11 [1]	1360.3	0.9	1.2	0.26	11 [1]						1351.9	6.3				25 [5]
																							1357.7	3.0				24 [1,5]
Weighted Mean (samples)		*6*	*1364.7*	*8.1*	*65*	*0.00*	*6 [5]*	*1360.4*	*4.6*	*21*	*0.00*	*6*	*1358.7*	*4.7*	*13*	*0.00*	*6*	*1364.4*	*6.5*	*95*	*0.00*	*6*	*1358.2*	*5.3*	*5.6*	*3.7*	*0.00*	*6*
		6	*1360.6*	*3.2*	*17*	*0.00*	*6 [1,5]*	*1360.4*	*3.8*	*19*	*0.00*	*6 [1,5]*											*1359.3*	*3.8*	*4.2*	*3.8*	*0.00*	*6 [5,9]*
		5																					*1357.5*	*1.8*	*2.5*	*0.9*	*0.45*	*5 [10]*
Weighted Mean (composite)		*114*	*1376.9*	*3.9*	*4.4*	*0.01*	*3 [5]*	*1356.2*	*0.7*	*1.7*	*0.11*	*7 [1,5]*	*1355.9*	*0.8*	*1.15*	*0.33*	*6 [1,5]*	*1359.7*	*0.3*	*1.5*	*0.09*	*16 [5]*	*1356.5*	*1.7*	*2.4*			*113 [1]*
																							1357.1	*1.7*	*2.4*			*96 [1,5]*
Gele	TB17-021-P1	20	1323.6	1.7	1.8	0.11	6 [5]	1306.9	5.1	n/a	n/a	1	1306.9	5.1	n/a	n/a	1	1316.6	1.3	1.2	0.33	5	1309.0	6.0				20
								1316.6	1.3	1.2	0.33	5	1316.6	1.3	1.2	0.33	5						1310.0	5.6				18 [5]
																							1314.6	3.1				17 [1,5]
	TB17-021-P2	18	1321.0	2.5	3.0	0.01	7 [5]	1318.0	1.1	0.7	0.69	7	1318.0	1.1	0.7	0.78	7	1318.0	1.1	0.6	0.78	8	1315.1	4.5				18
																							1315.7	2.6				15 [5]
	TB17-021-P3	10	1351.7	37.8	6.8	0.01	2 [5]	1322.6	4.4	1.9	0.15	3	1321.2	5.1	2.6	0.11	2	1322.6	4.4	1.9	0.15	3	1316.8	9.9				10
																							1317.6	8.2				8 [5]
Weighted Mea Weighted Mean		*3*	*1322.8*	*1.4*	*2.6*	*0.07*	*3 [5]*	*1317.8*	*7.5*	*12*	*0.00*	*3*	*1317.7*	*7.1*	*10*	*0.00*	*3*	*1317.7*	*3.5*	*4.0*	*0.02*	*3*	*1313.4*	*3.4*	*3.8*	*1.6*	*0.20*	*3*
			1317.6	*3.5*	*4.0*	*0.02*	*3 [5]*	*1317.6*	*0.8*	*2.4*	*0.09*	*3 [5]*											*1314.9*	*2.3*	*2.8*	*1.9*	*0.15*	*3 [5]*
																							1315.4	*1.9*	*2.5*	*0.3*	*0.75*	*3 [5,11]*
Weighted Mean (composite)		*48*	*1323.4*	*1.8*	*2.5*	*0.00*	*14 [5]*	1317.8	0.8	1.3	0.22	15 [1,5]	1317.2	1.3	2.1	0.01	14 [5]	*1317.8*	*0.8*	*1.3*	*0.22 [5]*	*15*	1315.4	2.4	2.9			47 [11]
																							1315.4	*2.0*	*2.6*			*40 [5,11]*

[1]Excl. youngest age; [2]Excl. TB17-009-P1; [3]Excl. 7822-47B; [4]Excl. youngest age of 7822-47A; [5]Excl. oldest 'gap' ages; [6]Excl. TB17-022-P3; [7]Excl. 81-201; [8]Excl. youngest age from TB17-022-P3; [9]Excl. youngest age from K82-787b; [10]excl. 81-219; [11]excl. youngest age from TB17-021-P1